Chapter 4

Coupling for a Translatory Armature

4.1 Introduction

The coupling for a translatory armature developed here, makes use of two independent orthogonal meshes. As an example, the moving and the fixed armature from the linear actuator presented in Fig. 4.1 are discretised in Finite Integration Technique as 3D models. From the beginning, we assume that the master model part is the fixed armature and the slave model part is the moving part.

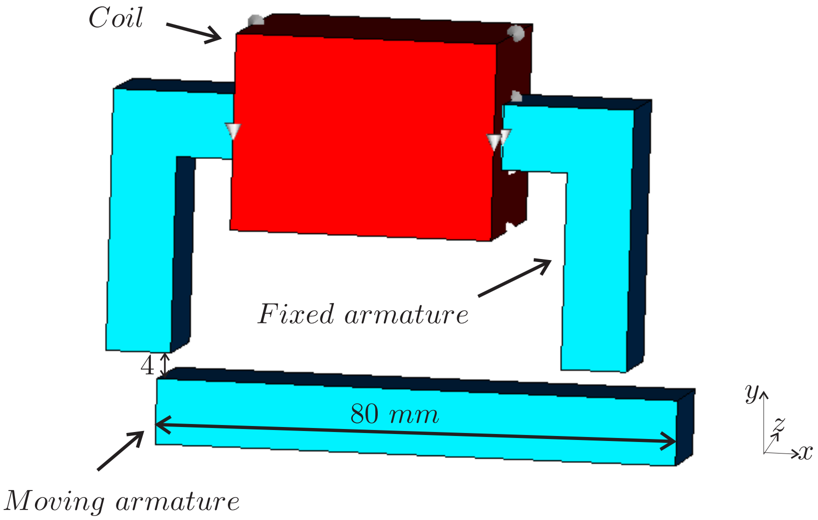

Figure 4.1: *Linear actuator.*

At the sliding surface, interface conditions are used, whereas at the outer part of the model homogeneous Dirichlet BCs are used (Fig. 4.2). In the case of translation, the portions at the interface that are not neighboring the other model part, *exterior interface conditions* are given, after case, periodic BC or homogeneous Dirichlet

BC. The model has to be long enough into the x-direction to allow the results to be uninfluenced by the electric BCs. The formulation couples the $\widehat{\mathbf{a}}_x$ and $\widehat{\mathbf{a}}_z$ components of the line-integrated magnetic vector potential allocated at the set of edges tangential to the common interface [70].

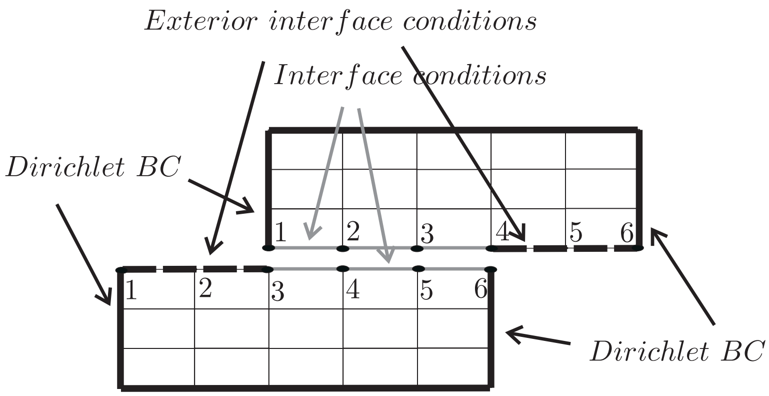

Figure 4.2: *Boundary and interface conditions applied on two equidistant and matching grids.*

The device is excited with a current $I = 10$ A applied to a coil with $N = 100$ turns. The fixed and the moving armatures are made from iron. The simulations in this chapter are done for a linear iron material with a relative permeability $\mu_r = 1000$.

4.2 Coupling Technique

The FIT model of the linear actuator contains the armature and the surrounding air. The moving part can be displaced both in x- and z-directions, along a plane parallel to the interface. The two considered coupling techniques used are the *locked-step approach* and the *linear interpolation* technique. Both are mathematically described by the equation:

$$\widehat{\mathbf{a}}_{\mathrm{slv},p} = \mathbf{k}_{\epsilon}\mathbf{k}^{0}_{\mathrm{shift}}\widehat{\mathbf{a}}_{\mathrm{mst},p}, \tag{4.1}$$

where $\widehat{\mathbf{a}}_{\mathrm{slv},p}$ and $\widehat{\mathbf{a}}_{\mathrm{mst},p}$ are the unknowns allocated at a set s_p of edges tangential to the slave and master sides of the interface (Fig. 4.3).

The shift operator $\mathbf{k}^{0}_{\mathrm{shift}}$ is responsible for the displacement related to an integer number of grid cells, whereas $\mathbf{k}_{\epsilon}$ is the linear interpolation operator, responsible for the fractional part of the displacement. For the locked-step approach, the matrix $\mathbf{k}_{\epsilon}$ is the identity matrix, as no fractional displacement is considered.

The 2D interpolation technique connects each degree of freedom from the slave side of the interface to at least 2 DOFs from the master side of the interface. This assumes that the meshes at both sides of the interface are staggered, or at least the mesh at the master side of the interface has no intermediate grid lines.

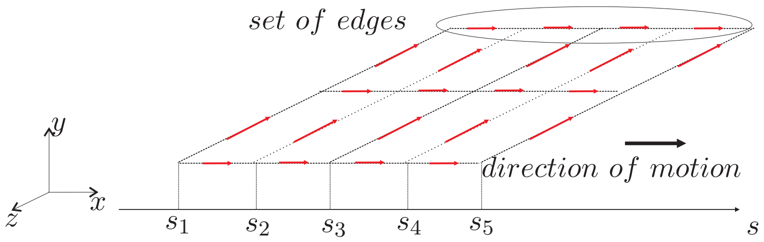

Figure 4.3: *Set of edges.*

For example, the displacement of a slightly non-equidistant grid including Dirichlet BCs, by 1 grid line corresponds to the $\mathbf{k}^0_{\text{shift}}$ operator:

$$\mathbf{k}^0_{\text{shift}} = \begin{bmatrix} 0 & 1 & 0 & ... & 0 \\ 0 & 0 & 1 & ... & 0 \\ ... & ... & ... & ... & ... \\ 0 & ... & 0 & 0 & 1 \\ 0 & ... & 0 & 0 & 0 \end{bmatrix} . \tag{4.2}$$

In Fig. 4.4 a) it is shown how the interpolation is carried out. Each slave DOF (with the x position $x_{s,i1}$, $i1 = 1...n$) is connected with 2 master DOFs ($x_{m,i}$, $x_{m,i+1}$) at the interface.

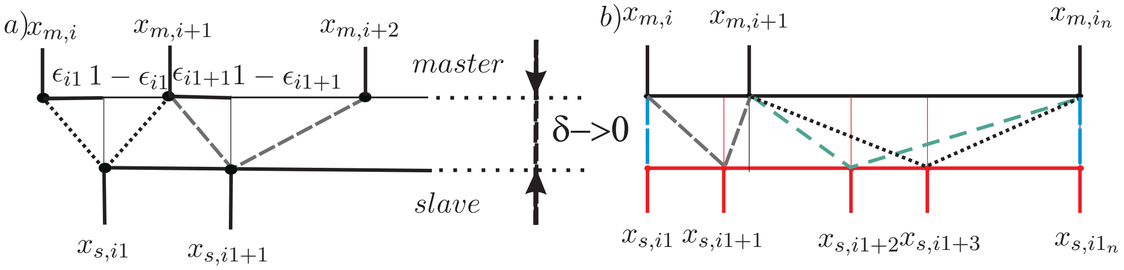

Figure 4.4: *Displacement of the moving armature with a fraction of a grid cell for: a) a slightly non-equidistant grid and b) an unregular grid at the slave side.*

The operator responsible for the displacement by a fraction of a grid line is

$$\mathbf{k}_\epsilon = \begin{bmatrix} 1-\epsilon_1 & \epsilon_1 & 0 & ... & 0 \\ 0 & 1-\epsilon_2 & \epsilon_2 & ... & 0 \\ ... & ... & ... & ... & ... \\ 0 & ... & 0 & 1-\epsilon_{n-1} & \epsilon_{n-1} \\ 0 & ... & 0 & 0 & 1-\epsilon_n \end{bmatrix} . \tag{4.3}$$

The fractional displacement ϵ_i for a single grid node is calculated by:

$$\epsilon_i = \frac{x_{s,i1} - x_{m,i}}{x_{m,i+1} - x_{m,i}} . \tag{4.4}$$

In the case of a matching grid Fig. 4.4 b), the first matching point has $\epsilon_1 = 0$ and the last matching point has $\epsilon_n = 1$.

When the grid is highly non-uniform, a staggered distribution of the master and slave grid lines as reflected by the two-diagonal structure presented in Eq. (4.3) is no longer guaranteed. The interpolation operator remains sparse, but is unstructured (Fig. 4.4 b)). In this case, dangling edges can occur, meaning that some of the edges at the master side remain uncoupled with respect to the slave side of the interface (Fig. 4.5).

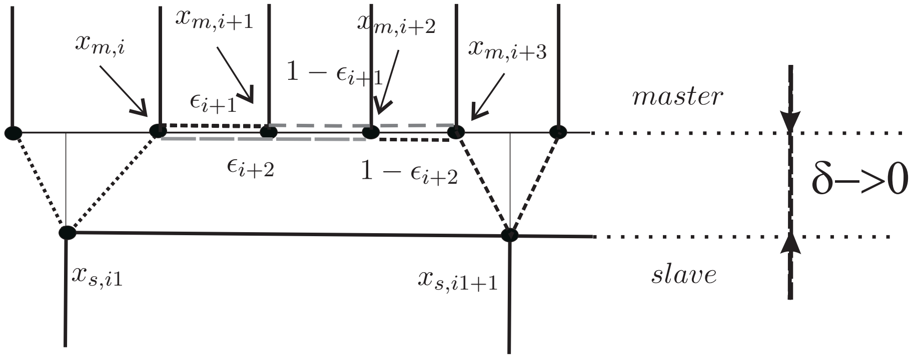

Figure 4.5: *Linear interpolation for dangling edges.*

Such DOFs will automatically experience a natural BCs, which here is equivalent to a magnetic BC and this mimic a boundary with an infinite permeability. This would cause large and unphysically magnetic fluxes at these boundary parts. To overcome this, the DOFs for these edges are linearly interpolated from DOFs of neighboring coupled edges. In this way some edges found at the master grid are transformed into slave edges.

The 2D interpolation for a staggered grid is made similar for both x- and z-directions (Fig. 4.6):

$$\epsilon_x = \frac{x_{s,i1} - x_{m,i}}{x_{m,i+1} - x_{m,i}} ; \tag{4.5}$$

$$\epsilon_z = \frac{z_{s,k1} - z_{m,k}}{z_{m,k+1} - z_{m,k}} . \tag{4.6}$$

The interpolation in x-direction is calculated by:

$$A_{\mathrm{z},s,i1,1} = (1-\epsilon_{\mathrm{x}})\ A_{\mathrm{z},m,i,k} + \epsilon_{\mathrm{x}}\ A_{\mathrm{z},m,i+1,k} ; \tag{4.7}$$

$$A_{\mathrm{z},s,i1,2} = (1-\epsilon_{\mathrm{x}})\ A_{\mathrm{z},m,i,k+1} + \epsilon_{\mathrm{x}}\ A_{\mathrm{z},m,i+1,k+1} ; \tag{4.8}$$

whereas the interpolation in z-direction is done from the previously interpolated x values:

$$A_{\mathrm{z},s,i1,k1} = (1-\epsilon_{\mathrm{z}})\ A_{\mathrm{z},s,i1,1} + \epsilon_{\mathrm{z}}\ A_{\mathrm{z},s,i1,2} . \tag{4.9}$$

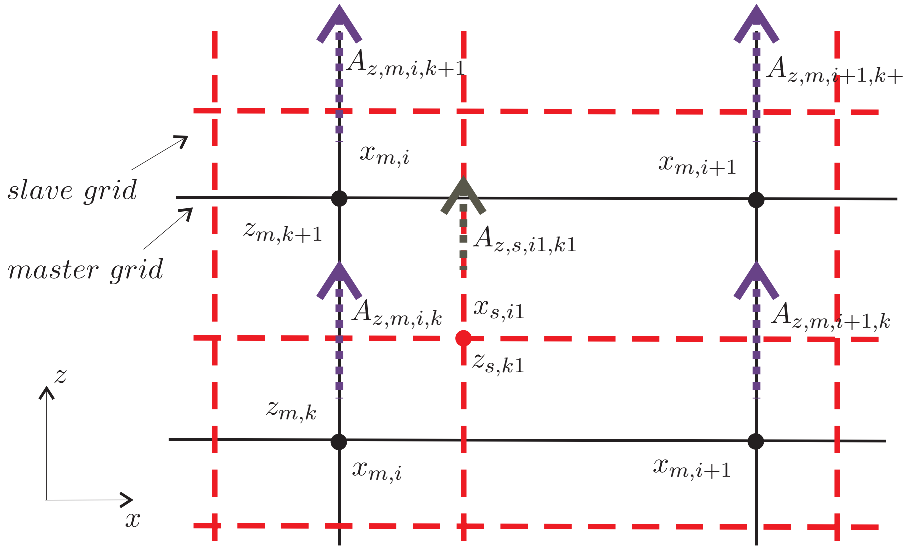

Figure 4.6: *Two-dimensional linear interpolation for a staggered grid.*

From Eq. (4.7), (4.8) and (4.9), the final interpolation formula reads:

$$\begin{aligned} A_{\mathrm{z},s,i1,k1} = {} & A_{\mathrm{z},m,i,k}\ (1-\epsilon_{\mathrm{x}})\ (1-\epsilon_{\mathrm{z}}) + A_{\mathrm{z},m,i,k+1}\ (1-\epsilon_{\mathrm{x}})\ \epsilon_{\mathrm{z}} + \\ & + A_{\mathrm{z},m,i+1,k}\ \epsilon_{\mathrm{x}}\ (1-\epsilon_{\mathrm{z}}) + A_{\mathrm{z},m,i+1,k+1}\ \epsilon_{\mathrm{x}}\ \epsilon_{\mathrm{z}}\ . \end{aligned} \tag{4.10}$$

In the linear system $\mathbf{K}\mathbf{u} = \mathbf{f}$, on the corresponding coefficient matrix $\mathbf{K} = \widetilde{\mathbf{C}}\mathbf{M}_{\nu}\mathbf{C}$ the BCs are applied. This is enforced by applying the projectors, as explained in Chapter 3, Section 3.3:

$$\mathbf{P}^H\mathbf{K}\mathbf{P}\mathbf{u} = \mathbf{P}^H\mathbf{f}\ . \tag{4.11}$$

Before coupling of the master and slave parts, the new system will have the expression

$$\begin{bmatrix} \mathbf{K}_{\mathrm{slv}} & 0 \\ 0 & \mathbf{K}_{\mathrm{mst}} \end{bmatrix} \begin{bmatrix} \widehat{\mathbf{a}}_{\mathrm{slv}} \\ \widehat{\mathbf{a}}_{\mathrm{mst}} \end{bmatrix} = \begin{bmatrix} \mathbf{f}_{\mathrm{slv}} \\ \mathbf{f}_{\mathrm{mst}} \end{bmatrix}\ . \tag{4.12}$$

The displacement of the moving part of the actuator influences the structure of the coefficient matrix and, implicit, the solving time.

Fig. 4.7 presents the structure of the coupled coefficient matrices for the non-displaced and displaced moving part of the actuator not-displaced or displaced in each of the x- or z-directions parallel to the coupling interface plane. As can be observed, the diagonal block structure of the coefficient matrix is damaged when the moving part is displaced in the z-direction.

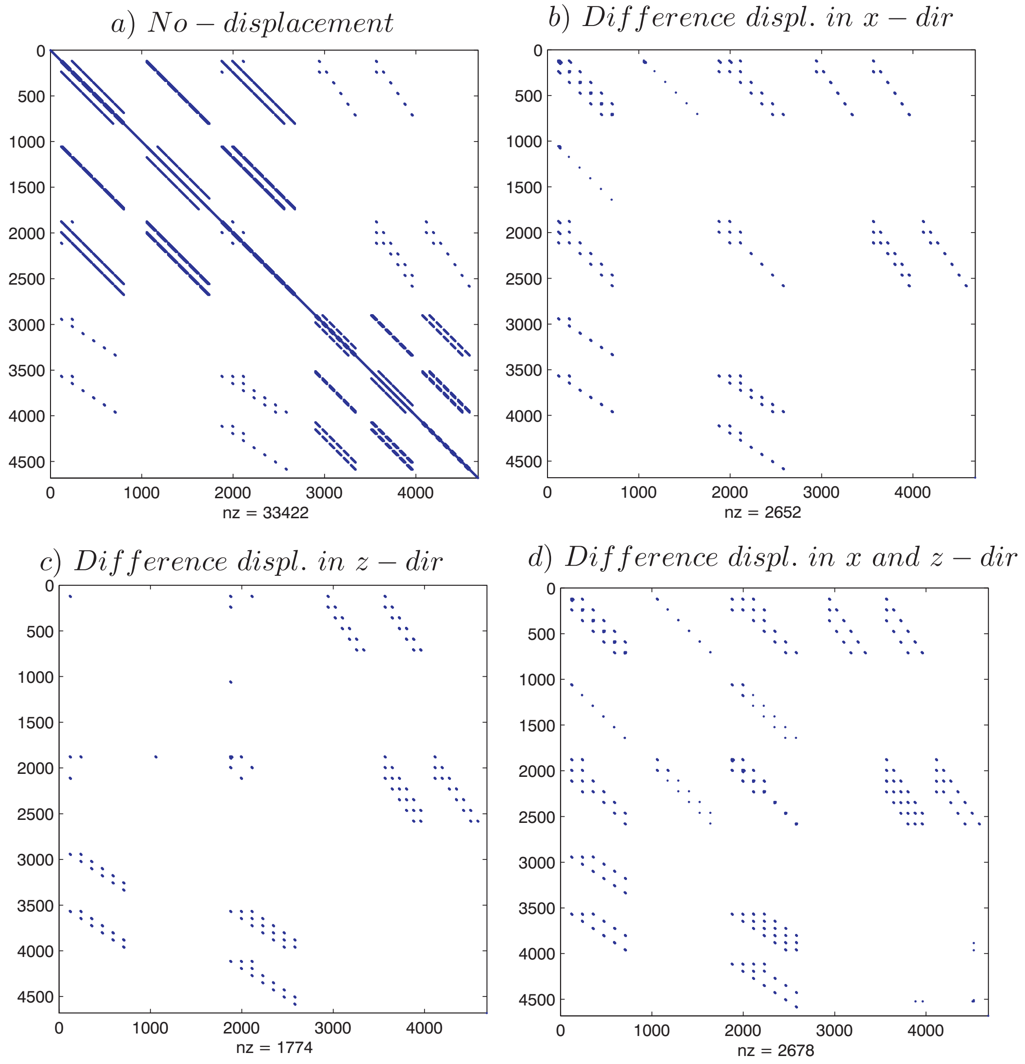

Figure 4.7: *Sparsity pattern of the coefficient matrix* **K** *a) without displacement, and the difference between displayed matrix and matrix without displacement: b) displacement in x-direction, c) displacement in z-direction and d) displacement in both x- and z-directions.*

4.3 Convergence Study

4.3.1 Analytical Model

In order to study the convergence of the coupling by linear interpolation, a comparison to an analytical model is setup. Two rectangular blocks are taken (Fig. 4.8). The upper block is fixed, whereas the lower block can be displaced in 2 directions. On the exterior part of the model, on the upper part of the fixed armature a potential is applied: $\hat{A}_{\mathrm{out}} \cos(k\ x)$, whereas for the $y_{\min}$, $z_{\min}$ and $z_{\max}$ homogeneous Dirichlet BCs are applied. On the $x_{\min}$ and $x_{\max}$ boundaries periodic BCs are applied.

On the sliding surface situated at the middle of the air gap, interface conditions

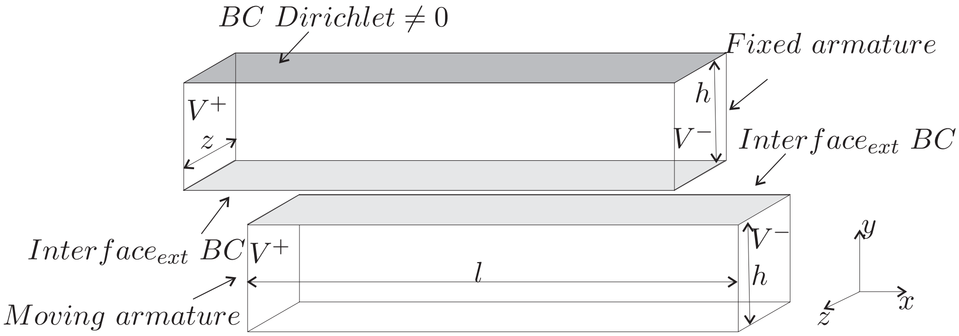

Figure 4.8: *Analytic model: boundary and interface conditions.*

are necessary. In case of a displacement, the exterior parts from the interface ($Interface_{\mathrm{ext}}$) get periodic BCs.

The z-component of the magnetic vector is written as:

$$A_{\mathrm{z}}(x,y) = (\alpha\ e^{ky} + \beta\ e^{-ky})\ \cos(kx)\ ; \tag{4.13}$$

with an entire period $l_{\mathrm{x}} = 2\pi/k$.

As the materials are homogeneous, we can write the curl-curl equation:

$$\nabla \times (\nu\ \nabla \times \mathbf{A}_{\mathrm{z}}) = 0\ , \Rightarrow \tag{4.14}$$

$$\frac{\partial^2 A_{\mathrm{z}}}{\partial x^2} + \frac{\partial^2 A_{\mathrm{z}}}{\partial y^2} = 0\ , \tag{4.15}$$

after derivation of Eq. (4.13):

$$\frac{\partial^2 A_z}{\partial x^2} = -k^2(\alpha\ e^{ky} + \beta\ e^{-ky})\ \cos(kx)\ ; \tag{4.16}$$

is obtained

$$\frac{\partial^2 A_z}{\partial y^2} = k^2(\alpha\ e^{ky} + \beta\ e^{-ky})\ \cos(kx)\ . \tag{4.17}$$

At the boundary y_{min} of the moving armature a homogeneous Dirichlet condition is applied. At the boundary $y_{\mathrm{max}} = h$ of the fixed armature, a nonzero potential is put. Then, Eq. (4.13) becomes:

$$A_{\mathrm{z}}(x, y = 0) = (\alpha + \beta)\ \cos(kx)\ ; \quad \Rightarrow \quad \alpha + \beta = 0 \tag{4.18}$$

$$A_{\mathrm{z}}(x, y = h) = (\alpha\ e^{kh} + \beta\ e^{-kh})\ \cos(kx)\ ; \quad \Rightarrow \quad (\alpha\ e^{kh} + \beta\ e^{-kh}) = A_{\mathrm{out}} \tag{4.19}$$

whereas the constants can be now extracted:

$$\alpha = \frac{A_{\mathrm{out}}}{e^{kh} + e^{-kh}}\ ; \tag{4.20}$$

$$\beta = -\alpha\ . \tag{4.21}$$

The moving part is displaced. The solution for the z-component of the magnetic vector potential is plotted in Fig. 4.9. (In order to see the difference, the scale of MVP is different for the fixed and for the moving armature.)

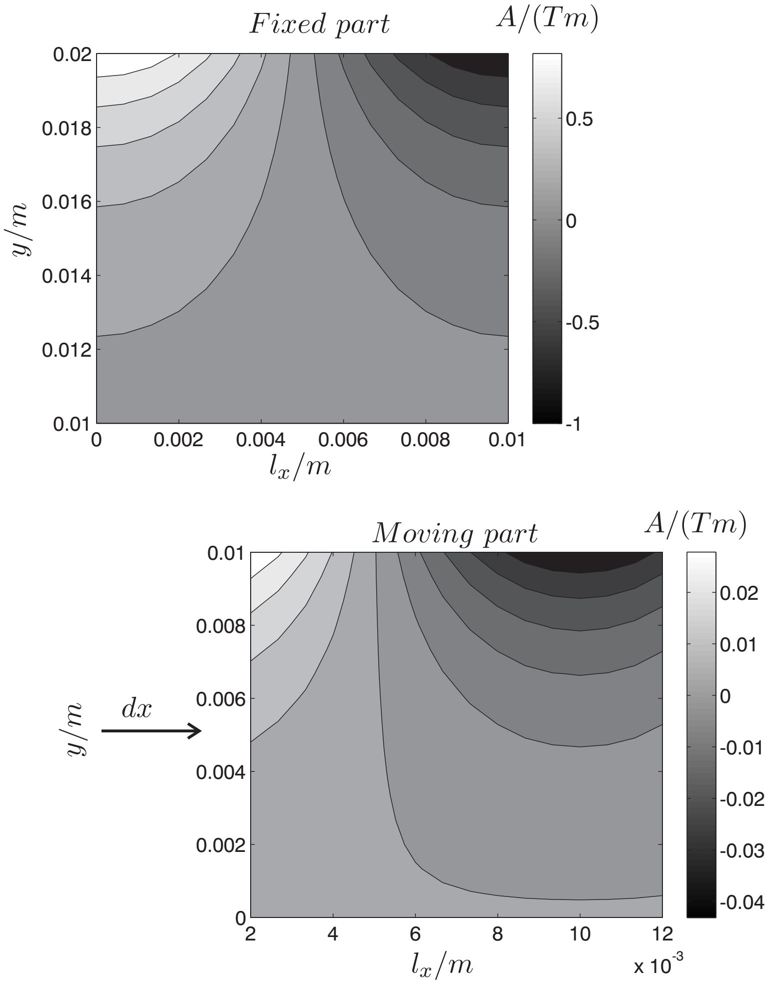

Figure 4.9: *Magnetic vector potential $\vec{A}$ for an analytical model with Dirichlet boundary conditions, displaced with dx in the x-direction.*

4.3.2 Discretization Error

The convergence of the discretization error can be either studied on the basis of the forces, either on the basis of the magnetic field. If the FIT model features a mirroring symmetry, the phenomenon of *happy cancelation of errors* can appear. Then, the forces obtained in FIT for the symmetrical grid are zero. In order to overcome this, an unsymmetric grid must be used.

Here, the discretization error is calculated for the magnetic field. Different numbers of DOFs are considered. The results for the coupled FIT model are compared to the results for the analytical model.

The relative error is:

$$\epsilon = \frac{\|\widehat{\mathbf{a}}_{\mathrm{FIT}} - \widehat{\mathbf{a}}_{\mathrm{analytic}}\|_2}{\|\widehat{\mathbf{a}}_{\mathrm{analytic}}\|_2} \,, \tag{4.22}$$

and is presented in Fig. 4.10 in the case of a non-displaced moving part. It can be observed that the convergence order is 2, as for the PMSM.

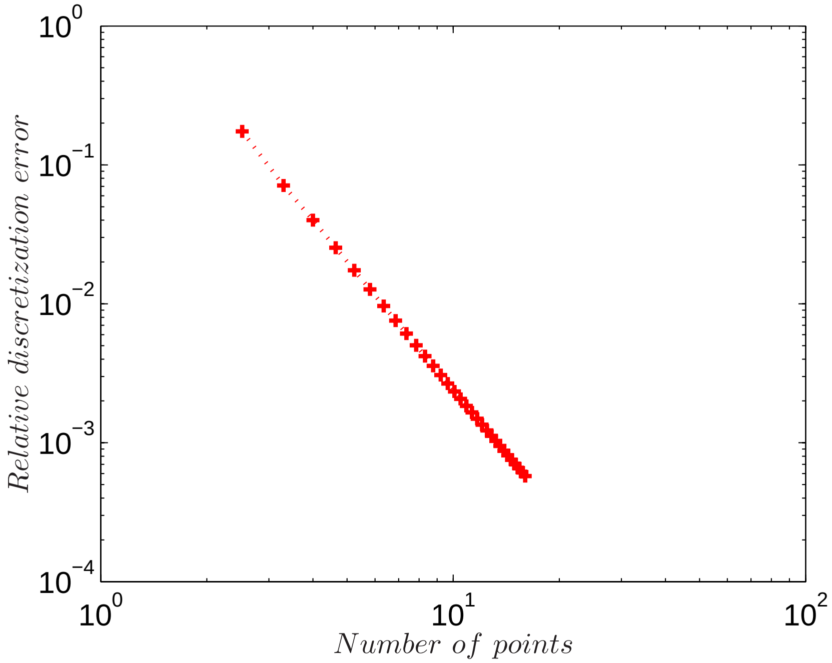

Figure 4.10: *2nd order convergence of the linear coupling.*

4.4 Force Computation by the Maxwell Stress Tensor Approach

During the last decades, different methods for the calculation of local and global forces in magnetized iron cores have been developed.

4.4.1 Conventional Maxwell Stress Tensor

The total force acting on any part of electrical device can be calculated from the magnetic field with the Maxwell stress tensor approach (4.23), with the Lorentz force technique (4.24) or with the virtual work method (4.25), which have proved to reach a high accuracy [55], [56]:

$$T = \frac{1}{\mu_0}\begin{bmatrix} B_\mathrm{x}^2 - \frac{1}{2}B^2 & B_\mathrm{x}B_\mathrm{y} & B_\mathrm{x}B_\mathrm{z} \\ B_\mathrm{y}B_\mathrm{x} & B_\mathrm{y}^2 - \frac{1}{2}B^2 & B_\mathrm{y}B_\mathrm{z} \\ B_\mathrm{z}B_\mathrm{x} & B_\mathrm{z}B_\mathrm{y} & B_\mathrm{z}^2 - \frac{1}{2}B^2 \end{bmatrix} ; \tag{4.23}$$

$$d\mathbf{F} = I(d\mathbf{l} \times \mathbf{B}) ; \tag{4.24}$$

$$F_s = \frac{\partial W_\mathrm{co}}{\partial s} . \tag{4.25}$$

The Maxwell stress tensor method is used for the calculation of the total force or the surface force distribution in electrical machines, but is not able to give any volume force distribution, since it considers only the surface integral, and describe the forces directly in terms of the magnetic field strength. The technique based on the Lorentz force treats the problem of a current-carrying conductor of length l, whereas the virtual work computes the force F_s in the direction of the displacement by calculating the variation of the stored co-energy in the model.

On the FIT grid, the components B_{x}, B_{y} and B_{z} of the magnetic field density are allocated at the primary facets of the grid (Fig. 4.11). These have to be interpolated upon a common set of facets in order to use the classical Maxwell stress tensor approach, and then to calculate the force as a divergence of the Maxwell tensor:

$$F = \nabla \cdot T \ . \tag{4.26}$$

The classical Maxwell stress tensor approach requires all three components of $\mathbf{B}$ to be available in a number of integration points, for example in the points where B_y is defined. These points are located at the primary faces, that coincide with the integration plane.

The results of the simulations are the line-integrated magnetic vector potentials $\widehat{\mathbf{a}}$. From $\widehat{\mathbf{a}}$, the magnetic fluxes $\widehat{\widehat{\mathbf{b}}}$ are obtained by $\widehat{\widehat{\mathbf{b}}} = \mathbf{C}\widehat{\mathbf{a}}$. This vector is decomposed in the components $\widehat{\widehat{\mathbf{b}}}_x$,$\widehat{\widehat{\mathbf{b}}}_y$ and $\widehat{\widehat{\mathbf{b}}}_z$, from which B_x, B_y and B_z are obtained by dividing through the facet areas. The components B_x and B_z are brought at the same position

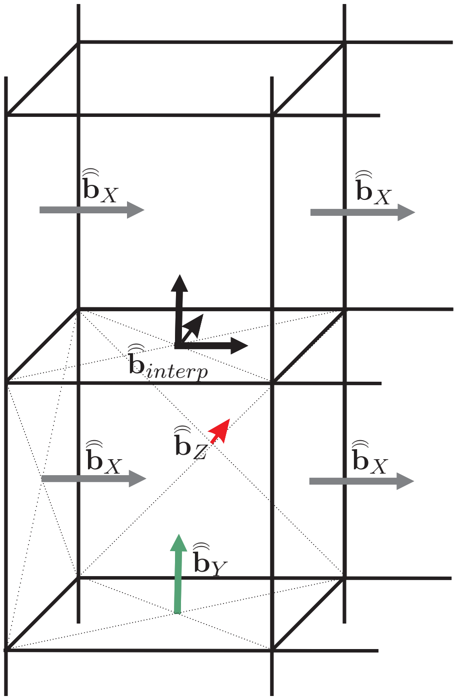

Figure 4.11: *Allocation of the magnetic fluxes at the primary facets* $\widehat{\widehat{\mathbf{b}}}$*; interpolation of the magnetic flux at the y-facet.*

as B_y by bilinear interpolation:

$$B_x = \frac{\frac{B_x(q)+B_x(q+1)}{2}\, d_y(j) + \frac{B_x(q-nx)+B_x(q+1-nx)}{2}\, d_y(j-1)}{d_y(j) + d_y(j-1)} \; ; \tag{4.27}$$

$$B_z = \frac{\frac{B_z(q)+B_z(q+nx\ ny)}{2}\, d_y(j) + \frac{B_z(q-nx)+B_z(q-nx+nx\ ny)}{2}\, d_y(j-1)}{d_y(j) + d_y(j-1)} \; ; \tag{4.28}$$

with $q = i + (j-1)\ nx + (k-1)\ nx\ ny$ (see Chapter 2).

The forces are:

$$F_x = \int_A \frac{B_x B_y}{\mu_0}\, dA \; ; \tag{4.29}$$

$$F_z = \int_A \frac{B_z B_y}{\mu_0}\, dA \; ; \tag{4.30}$$

$$F_y = \int_A \left(\frac{B_y^2}{2\mu_0} - \frac{B_x^2}{2\mu_0} - \frac{B_z^2}{2\mu_0}\right) dA \; ; \tag{4.31}$$

where A is the area that envelopes the mobile armature.

4.4.2 Fast Fourier Transform

In the case of an equidistant grid, the force can be calculated at the interface using 2D Fast Fourier Transforms.

For calculating the force, the field is decomposed in its Fourier coefficients, the Maxwell stress tensor is constructed and the interpolation is carried out analytically. In practice, the process consists of the identification of the coefficients $a_{\lambda,\xi}$ and $b_{\lambda,\xi}$ of a semi-analytical solution for the magnetic scalar potential calculated between two mesh planes situated in the air gap region (Fig. 4.12):

$$\Psi(x,y,z) = \sum_{\lambda}\sum_{\xi} e^{\jmath\lambda x}\, e^{\jmath\xi z}\left(a_{\lambda,\xi}\cosh(\zeta y) + b_{\lambda,\xi}\sinh(\zeta y)\right) . \tag{4.32}$$

The indices $\lambda = \frac{2\pi}{T_x}(i-1)$ and $\xi = \frac{2\pi}{T_z}(k-1)$, where T_x and T_z are the dimensions of the air gap in x- and z-direction, i and k are harmonic order, and $\zeta = \sqrt{\lambda^2 + \xi^2}$.

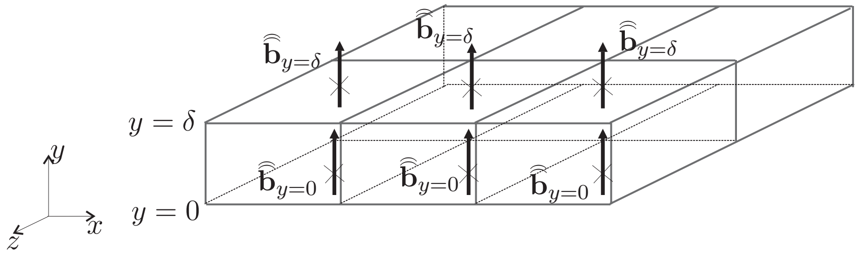

Figure 4.12: *Analytical model domain.*

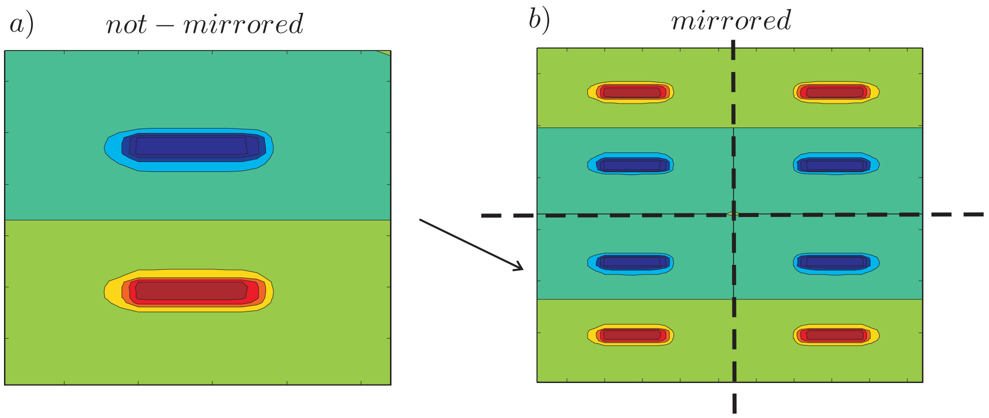

Figure 4.13: *Magnetic field a) on stator and b) mirrored field.*

The magnetic flux density is:

$$\mathbf{B} = (B_x, B_y, B_z) = (-\mu_0 \frac{\partial \Psi}{\partial x}, -\mu_0 \frac{\partial \Psi}{\partial y}, -\mu_0 \frac{\partial \Psi}{\partial z}) \ . \tag{4.33}$$

To apply Fast Fourier Transforms, a periodic field is necessary. Due to the fact that the model is not periodic, the magnetic field must be mirrored. In this way, the number of points is multiplied by four (Fig. 4.13).

In integral form, the forces in the x, y and z-direction are:

$$F_x = \int_0^{T_x/2} \int_0^{T_z/2} B_y^* H_x \, dxdz \ ; \tag{4.34}$$

$$F_y = \int_0^{T_x/2} \int_0^{T_z/2} (\frac{B_y^2}{2\mu_0} - \frac{B_x^2}{2\mu_0} - \frac{B_z^2}{2\mu_0}) \, dxdz \ ; \tag{4.35}$$

$$F_z = \int_0^{T_x/2} \int_0^{T_z/2} B_y^* H_z \, dxdz \ . \tag{4.36}$$

The component B_y of Eq. (4.33):

$$B_y = -\mu_0 \sum_{\lambda} \sum_{\xi} \zeta e^{\jmath \lambda x} \ e^{\jmath \xi z} (a_{\lambda,\xi} \sinh(\zeta y) + b_{\lambda,\xi} \cosh(\zeta y)) \tag{4.37}$$

is evaluated at two distinct planes in the air gap ($y = 0$ and $y = \delta$) and is written as function of the Fourier coefficients $d_y(i,k)$:

$$B_y(i,k) = \sum_{\lambda} \sum_{\xi} d_y(i,k) e^{\jmath \lambda x} \ e^{\jmath \xi z} \ . \tag{4.38}$$

The Fourier coefficients $a_{\lambda,\xi}$ and $b_{\lambda,\xi}$ are identified from the Fourier coefficients $d_{y=0}$ for the magnetic flux densities B_y at the plane $y = 0$ and from the Fourier coefficients

$d_{y=\delta}$ for the plane $y = \delta$:

$$b_{\lambda,\xi} = -\frac{d_{y=0}}{\mu_0\ \zeta}\ ; \tag{4.39}$$

$$a_{\lambda,\xi} = -\frac{d_{y=\delta}}{\mu_0\ \zeta \sinh(\zeta\delta)} - \frac{b_{\lambda,\xi}\cosh(\zeta\delta)}{\sinh(\zeta\delta)}\ . \tag{4.40}$$

Introducing the Fourier coefficients in the Eq. (4.33) the two other components of the magnetic flux density are obtained:

$$B_x = -\jmath\mu_0 \sum_\lambda \sum_\xi \lambda e^{\jmath\lambda x}\ e^{\jmath\xi z}(a_{\lambda,\xi}\cosh(\zeta y) + b_{\lambda,\xi}\sinh(\zeta y))\ ; \tag{4.41}$$

$$B_z = -\jmath\mu_0 \sum_\lambda \sum_\xi \xi e^{\jmath\lambda x}\ e^{\jmath\xi z}(a_{\lambda,\xi}\cosh(\zeta y) + b_{\lambda,\xi}\sinh(\zeta y))\ . \tag{4.42}$$

The Maxwell stress tensor is integrated in the x- and z-direction only at a quarter of the domain. The Eq. (4.34) and (4.36) result in:

$$F_x = \sum_\lambda \sum_\xi \sum_{\lambda'} \sum_{\xi'} \jmath\mu_0\ \lambda a_{\lambda,\xi}\ \zeta' b^*_{\lambda',\xi'} \int_0^{T_x/2} e^{\jmath(\lambda-\lambda')x}dx \int_0^{T_z/2} e^{\jmath(\xi-\xi')z}dz; \tag{4.43}$$

$$F_z = \sum_\lambda \sum_\xi \sum_{\lambda'} \sum_{\xi'} \jmath\mu_0\ \xi a_{\lambda,\xi}\ \zeta' b^*_{\lambda',\xi'} \int_0^{T_x/2} e^{\jmath(\lambda-\lambda')x}dx \int_0^{T_z/2} e^{\jmath(\xi-\xi')z}dz; \tag{4.44}$$

with the integrals:

$$\int_0^{T_x/2} e^{\jmath(\lambda-\lambda')x}dx = \begin{cases} \frac{-1+e^{\jmath(\lambda-\lambda')T_x/2}}{\jmath(\lambda-\lambda')} & : \text{ for } \lambda \neq \lambda' \\ \frac{T_x}{2} & : \text{ for } \lambda = \lambda' \end{cases} ; \tag{4.45}$$

$$\int_0^{T_z/2} e^{\jmath(\xi-\xi')z}dz = \begin{cases} \frac{-1+e^{\jmath(\xi-\xi')T_z/2}}{\jmath(\xi-\xi')} & : \text{ for } \xi \neq \xi' \\ \frac{T_z}{2} & : \text{ for } \xi = \xi' \end{cases} . \tag{4.46}$$

The y component of the force is:

$$F_y = \int_0^{T_x} e^{\jmath(\lambda-\lambda')x}dx \int_0^{T_z} e^{\jmath(\xi-\xi')z}dz\ \frac{1}{2}\mu_0(\zeta^2 b_{\lambda,\xi}b^*_{\lambda,\xi} - \lambda^2 a_{\lambda,\xi}a^*_{\lambda,\xi} - \xi^2 a_{\lambda,\xi}a^*_{\lambda,\xi})\ . \tag{4.47}$$

In case of a periodic model, the sums can be simplified up to:

$$F_y = \frac{1}{4}\sum_\lambda \sum_\xi \frac{1}{2}\mu_0(\zeta^2 b_{\lambda,\xi}b^*_{-\lambda,-\xi} - \lambda^2 a_{\lambda,\xi}a^*_{-\lambda,-\xi} - \xi^2 a_{\lambda,\xi}a^*_{-\lambda,-\xi})T_x T_z\ . \tag{4.48}$$

The force calculation with Fast Fourier Transform must be carried out on an *equidistant mesh*. For a non-equidistant mesh of the model, a *virtual* equidistant grid is

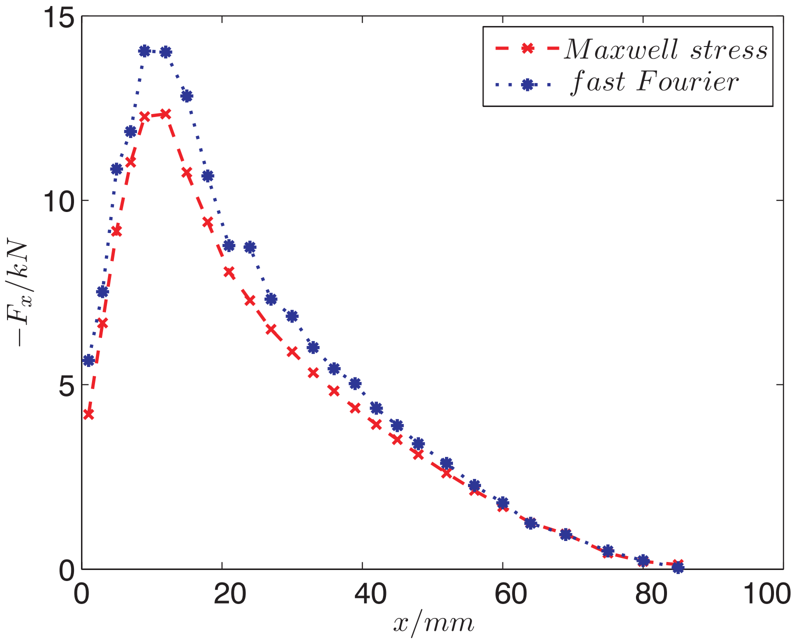

Figure 4.14: *Force calculation: comparison between the Maxwell stress tensor approach and the Maxwell stress tensor approach with fast Fourier transform.*

made at the interface, both for the master and the slave side of the model. The magnetic field will be interpolated on this virtual equidistant grid.

A comparison was made between the generated forces calculated both by the Maxwell stress tensor and the Maxwell stress tensor approach with Fast Fourier Transform for a displacement of the mobile armature in the x-direction (Fig.4.14).

The FFT approach for the Maxwell stress tensor result is especially for displacements bigger than 15 mm not very smooth as the classical Maxwell stress tensor. The 2D interpolation applied on the FIT grid in order to obtain an equidistant mesh can be responsible for this variation.

Chapter 5

Transient Simulation of Linear Actuators

5.1 Linear Actuator

The fixed and the moving part of a 3D linear actuator (Fig. 5.1) are independently discretised by FIT and are connected to each other at a common surface in the air gap.

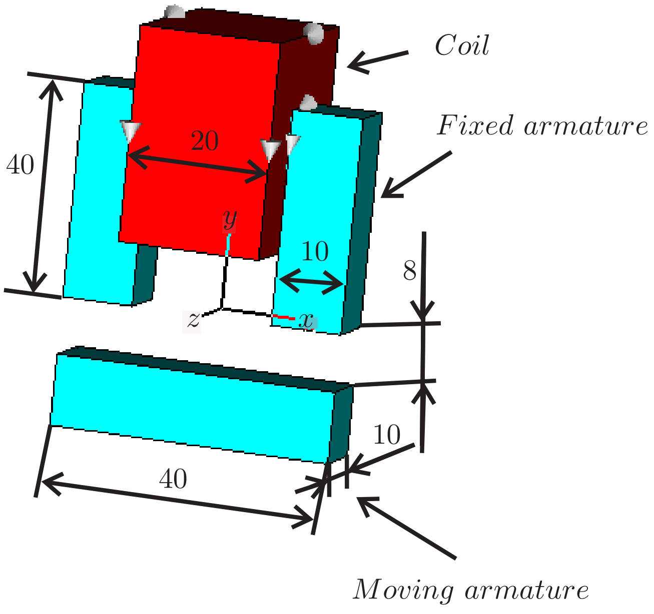

Figure 5.1: *Linear actuator - construction data.*

The FIT model (containing the moving armature, the surrounding air and half of the air gap) can be displaced in both x- and $z-$direction, with respect to a plane parallel to the coupling interface (Fig. 5.2).

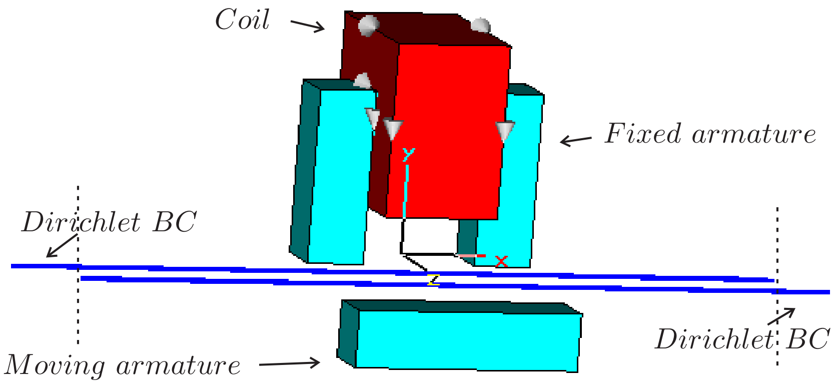

Figure 5.2: *Linear actuator - simulation domain (as a rule of thumb, the extent of the surrounding air fraction in both left and right x-direction are taken to be as large as the actuator itself) and applied boundary conditions.*

The magnetostatic formulation in terms of the magnetic vector potential integrated along primary edges, $\widehat{\mathbf{a}}$, discretised by the FIT, reads:

$$\widetilde{\mathbf{C}}\mathbf{M}_\nu\mathbf{C}\widehat{\mathbf{a}} = \widehat{\widehat{\mathbf{j}}}_s + \widetilde{\mathbf{C}}\mathbf{M}_\nu\widehat{\widehat{\mathbf{b}}}_\mathrm{r} \ , \tag{5.1}$$

where $\mathbf{C}$ and $\widetilde{\mathbf{C}}$ represent the discrete curl matrices at the primary and dual grid respectively, $\widehat{\widehat{\mathbf{j}}}_\mathrm{s}$ is the current density applied in the coils of the fixed armature, $\widetilde{\mathbf{C}}\mathbf{M}_\nu\widehat{\widehat{\mathbf{b}}}_\mathrm{r}$ is the contribution of the permanent magnet (in this example, there is no magnet excitation) and $\mathbf{M}_\nu$ is the reluctivity matrix. All the assumptions made in the previous Chapter 4 about the coupling and boundary conditions, maintain.

5.1.1 Influence of the Boundary

The boundary conditions (BCs) have a very big influence on the calculation results. For example, if a Dirichlet BC is applied at the exterior of the model, the magnetic flux lines are parallel to the boundary. If the boundary is not situated far enough from the device, the magnetic flux lines are forced to remain within the model. The values of the force calculated with the Maxwell stress tensor for a non-displaced actuator, according to Fig. 5.4, with Dirichlet BC are presented in the Table 5.1.

Table 5.1: *Convergence of the force with respect to the distance of the boundary conditions - according to Fig. 5.4.*

	a) $x = 80\ mm$	b) $x = 120\ mm$	c) $x = 200\ mm$
$F_x\ [N]$	$-0.22929\ 10^{-6}$	$-0.18186\ 10^{-6}$	$-0.08042\ 10^{-6}$
$F_y\ [N]$	$1.14465\ 10^{0}$	$0.99946\ 10^{0}$	$0.94586\ 10^{0}$
$F_z\ [N]$	$-0.05621\ 10^{-6}$	$-0.03713\ 10^{-6}$	$-0.03426\ 10^{-6}$

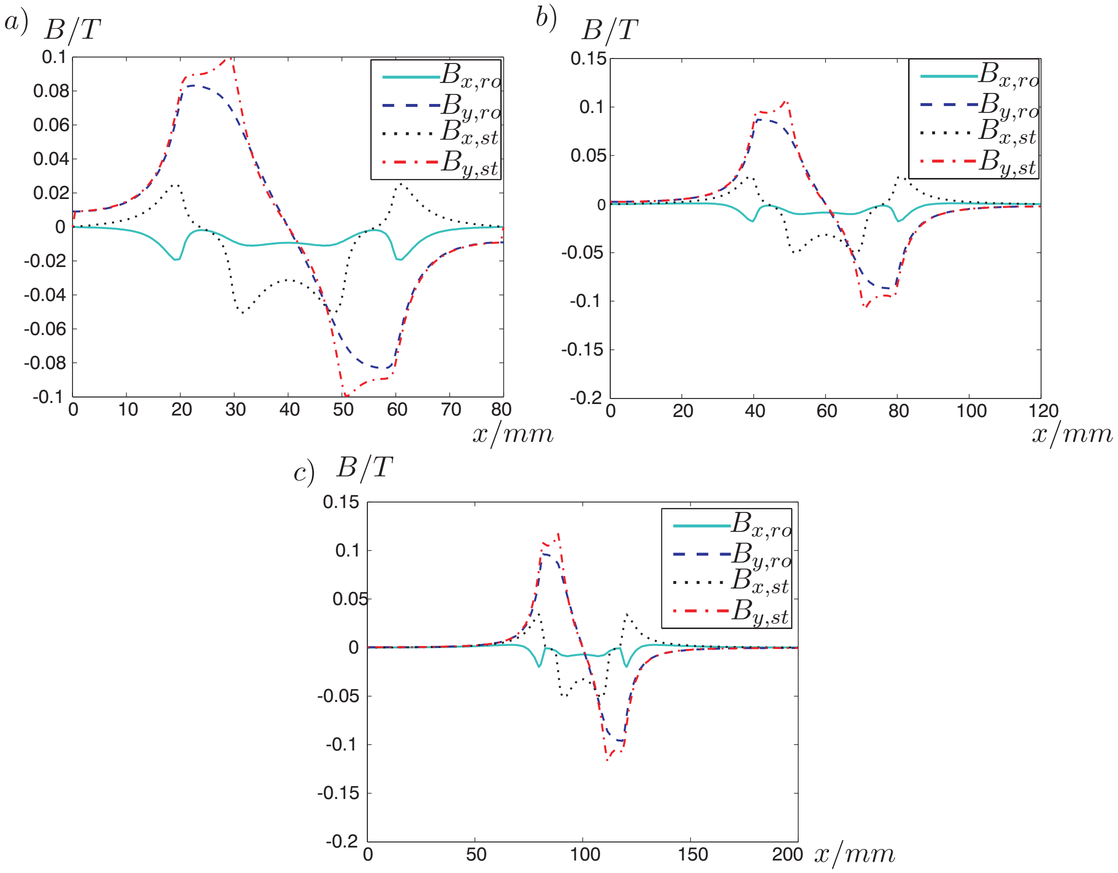

Figure 5.3: *B_x and B_y along a line in the x-direction in the middle of the air gap for a computational domain of linear actuator with a length in x-direction: a) 80 mm; b) 120 mm; c) 200 mm.*

5.1.2 Time Integration

When the iron from the moving part is conductive, eddy currents are induced due to the movement. In this case, the magnetoquasistatic Eq. (3.6) becomes

$$\widetilde{\mathbf{C}}\mathbf{M}_\nu\mathbf{C}\widehat{\mathbf{a}}(t) + \mathbf{M}_\kappa\frac{d\widehat{\mathbf{a}}(t)}{dt} = \widehat{\widehat{\mathbf{j}}}_s(t)\ . \tag{5.2}$$

The integrated magnetic vector potentials $\widehat{\mathbf{a}}$ are the unknowns in the models, $\mathbf{M}_\nu$ is the reluctivity matrix, $\mathbf{M}_\kappa$ is the conductivity matrix and $\widehat{\widehat{\mathbf{j}}}_s$ is the source current.

A time integrator based on the *Theta-method* is used [54]. The discretization of $\widehat{\mathbf{a}}$ and its time derivative read:

$$\widehat{\mathbf{a}} = \theta\widehat{\mathbf{a}}^{(n+1)} + (1-\theta)\widehat{\mathbf{a}}^{(n)}\ ; \tag{5.3}$$

$$\frac{d\widehat{\mathbf{a}}}{dt} = \frac{\widehat{\mathbf{a}}^{(n+1)} - \widehat{\mathbf{a}}^{(n)}}{\Delta t}\ . \tag{5.4}$$

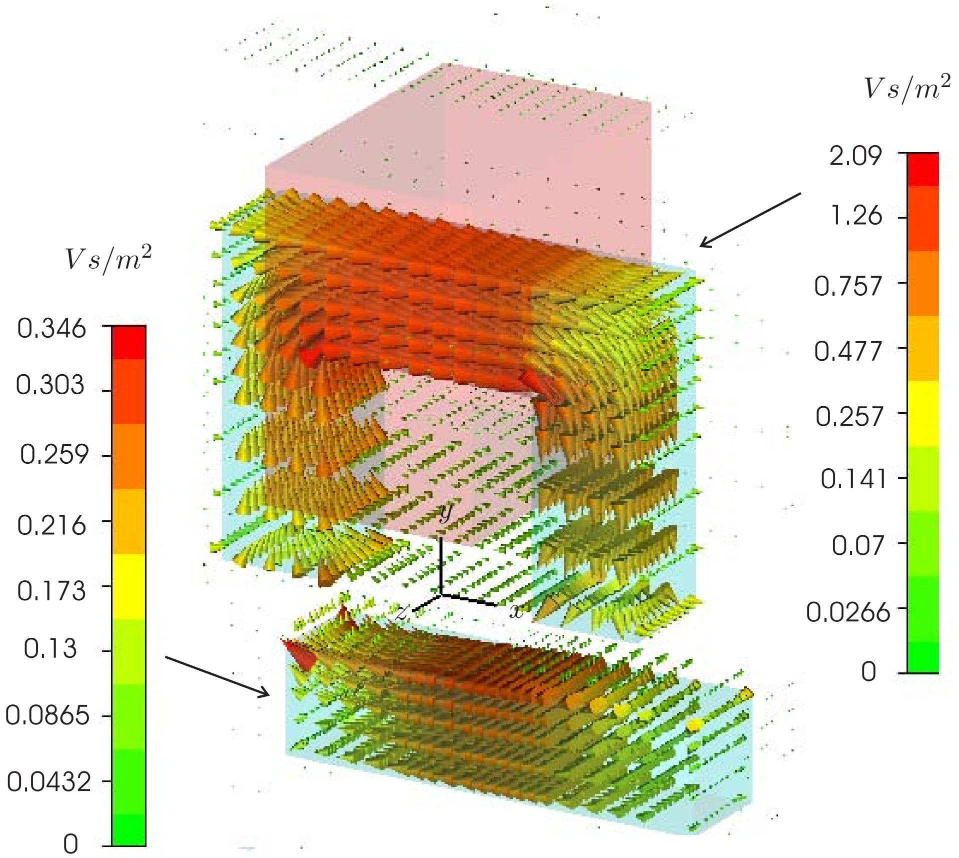

Figure 5.4: *Magnetic field density arrows for an actuator with linear material displaced in the x-direction, solved by DIDO and the results plotted in EM Studio.*

Hence, Eq. (5.2) becomes

$$\widetilde{\mathbf{C}}\mathbf{M}_\nu\mathbf{C}(\theta\widehat{\mathbf{a}}^{(n+1)} + (1-\theta)\widehat{\mathbf{a}}^{(n)}) + \frac{\mathbf{M}_\kappa}{\Delta t}(\widehat{\mathbf{a}}^{(n+1)} - \widehat{\mathbf{a}}^{(n)}) \\ = \theta\widehat{\widehat{\mathbf{j}}}^{(n+1)} + (1-\theta)\widehat{\widehat{\mathbf{j}}}^{(n)}, \quad (5.5)$$

with a time step $\Delta t = t^{(n+1)} - t^{(n)}$ and the vector at the new time instant denoted by $\widehat{\mathbf{a}}^{(n+1)} = \widehat{\mathbf{a}}(t^{(n)} + \Delta t)$.

Depending on the Θ parameter values, four particular Theta-method are distinguished:
$\Theta = 1$ - Implicit (backward) Euler;
$\Theta = 1/2$ - Crank-Nicolson;
$\Theta = 2/3$ - Galerkin;
$\Theta = 0$ - Explicit (forward) Euler.

For the simulations carried out below, the implicit backward Euler is selected as integration method, and the system of equations is:

$$\left[\widetilde{\mathbf{C}}\mathbf{M}_\nu\mathbf{C} + \frac{\mathbf{M}_\kappa}{\Delta t}\right]\widehat{\mathbf{a}}^{(n+1)} = \widehat{\widehat{\mathbf{j}}} + \frac{\mathbf{M}_\kappa}{\Delta t}\widehat{\mathbf{a}}^{(n)} \ . \quad (5.6)$$

The decoupled system of equations obtained by independently discretising both FIT models reads:

$$\begin{bmatrix} \mathbf{K}_{\mathrm{fx}} & 0 \\ 0 & \mathbf{K}_{\mathrm{mv}} \end{bmatrix} \begin{bmatrix} \widehat{\mathbf{a}}_{\mathrm{fx}}^{(n+1)} \\ \widehat{\mathbf{a}}_{\mathrm{mv}}^{(n+1)} \end{bmatrix} + \begin{bmatrix} \mathbf{g}_{\mathrm{fx}}^{(n+1)} \\ \mathbf{g}_{\mathrm{mv}}^{(n+1)} \end{bmatrix} = \begin{bmatrix} \widehat{\widehat{\mathbf{j}}}_{\mathrm{fx}} \\ 0 \end{bmatrix} + \begin{bmatrix} \frac{\mathbf{M}_{\kappa,\mathrm{fx}}}{\Delta t} & 0 \\ 0 & \frac{\mathbf{M}_{\kappa,\mathrm{mv}}}{\Delta t} \end{bmatrix} \begin{bmatrix} \widehat{\mathbf{a}}_{\mathrm{fx}}^{(n)} \\ \widehat{\mathbf{a}}_{\mathrm{mv}}^{(n)} \end{bmatrix} \tag{5.7}$$

where

$$\mathbf{K}_{\mathrm{fx}} = \widetilde{\mathbf{C}}_{\mathrm{fx}} \mathbf{M}_{\nu,\mathrm{fx}} \mathbf{C}_{\mathrm{fx}} + \frac{\mathbf{M}_{\kappa,\mathrm{fx}}}{\Delta t} \ ; \tag{5.8}$$

$$\mathbf{K}_{\mathrm{mv}} = \widetilde{\mathbf{C}}_{\mathrm{mv}} \mathbf{M}_{\nu,\mathrm{mv}} \mathbf{C}_{\mathrm{mv}} + \frac{\mathbf{M}_{\kappa,\mathrm{mv}}}{\Delta t} \ ; \tag{5.9}$$

are the system matrices of the fixed and moving armatures, respectively. The unknown vector $\mathbf{g}_{\mathrm{fx}}^{(n+1)}$ and $\mathbf{g}_{\mathrm{mv}}^{(n+1)}$ represent the magnetic voltage exerted by both models parts upon each other at the interface in the air-gap.

5.2 Mechanical Equation

In order to simulate the movement of the actuator, the kinetic properties are implemented. The equation for the damped oscillation of a mechanical system can be written as:

$$m\frac{d^2x}{dt^2} + c\frac{dx}{dt} + kx = F_x \ , \tag{5.10}$$

where m is the mass of the moving armature, c is the damping coefficient and k is the spring coefficient. F_x is the force in x-direction, computed by the Maxwell stress tensor [69]. The first term in the left hand side represents the force needed to overcome inertia, the second term overcomes the friction and the third is the spring force.

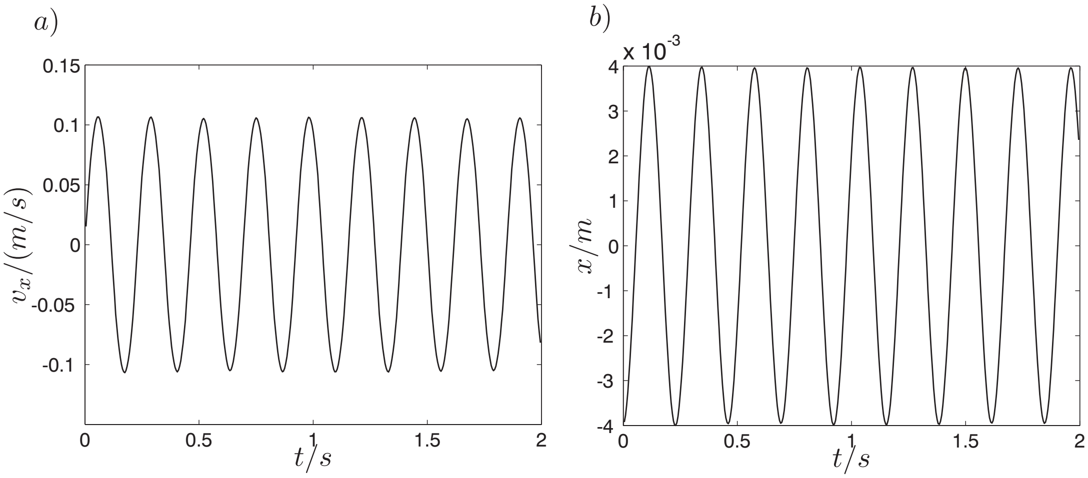

Figure 5.5: *a) Speed v_x and b) displacement in x-direction for non-amortisated oscillation.*

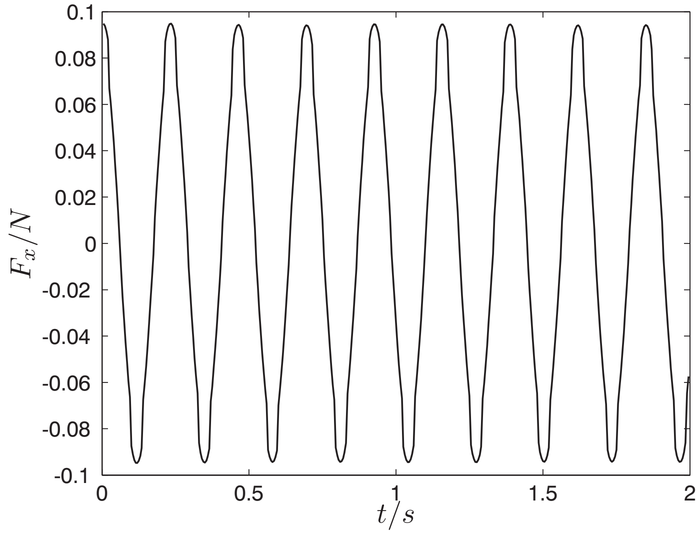

Figure 5.6: *Force in x-direction F_x for non-amortisated oscillation.*

The mechanical equation can be written as a system of first order differential equation:

$$\frac{d}{dt}\begin{bmatrix} x(t) \\ v_x(t) \end{bmatrix} = \begin{bmatrix} 0 & 1 \\ \frac{-k}{m} & \frac{-c}{m} \end{bmatrix}\begin{bmatrix} x(t) \\ v_x(t) \end{bmatrix} + \begin{bmatrix} 0 \\ \frac{F_x(t)}{m} \end{bmatrix}. \tag{5.11}$$

Eq. (5.11) becomes by discrete differentiation:

$$\begin{bmatrix} x^{(k+1)} \\ v_x^{(k+1)} \end{bmatrix} = \begin{bmatrix} x^{(k)} \\ v_x^{(k)} \end{bmatrix} + \Delta t \begin{bmatrix} 0 & 1 \\ \frac{-k}{m} & \frac{-c}{m} \end{bmatrix}\begin{bmatrix} x^{(k)} \\ v_x^{(k)} \end{bmatrix} + \Delta t \begin{bmatrix} 0 \\ \frac{F_x^{(k)}}{m} \end{bmatrix}, \tag{5.12}$$

with the time step $\Delta t \ll 1$.

If the terms c and k are zero in the Eq. (5.10), a non-amortisated oscillation for the speed, the displacement and the force will be obtained (Fig. 5.5 and Fig. 5.6). If the

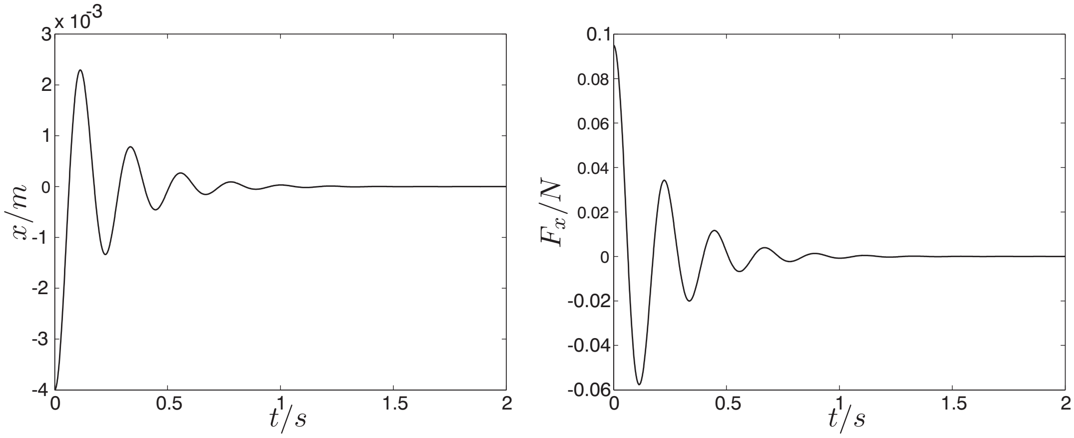

Figure 5.7: *Displacement x and force F_x for a dampened mechanical system with a small time constant (c=0.3).*

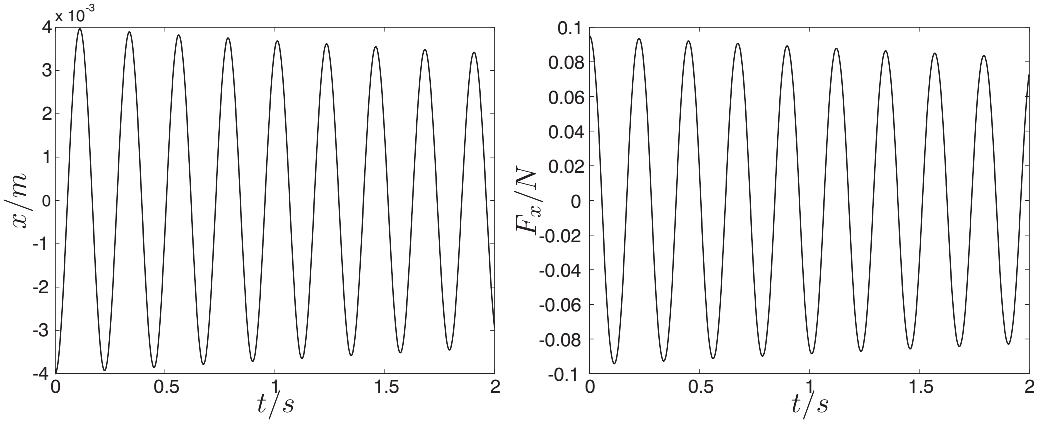

Figure 5.8: *Displacement x and force F_x for a mechanical system with a large time constant (c=0.005).*

damping constant is not zero, a time amortisated oscillation will appear. Depending whether a small or a big value of damping constant c is used, the amortisation will be fast or slow, as it can be seen in Fig. 5.7 and Fig. 5.8.

An analytical solution is obtained for the displacement x from the Eq. (5.10). The dependence of the force F_x on the displacement x is simulated on beforehand (Fig. 5.9). The behavior of the actuator with a DC current excitations can be interpreted as a nonlinear spring.

The mass of the moving armature is $m = V\rho$, with the volume: $V=10^{-2} \cdot 10^{-2} \cdot 4 \cdot 10^{-2}$ m^3 and the iron's density $\rho = 7.78$ g/cm^3, resulting a mass $m = 0.0311$ kg.

The spring k is considered to be zero, whereas the damping constant is $c = 0.0433$.

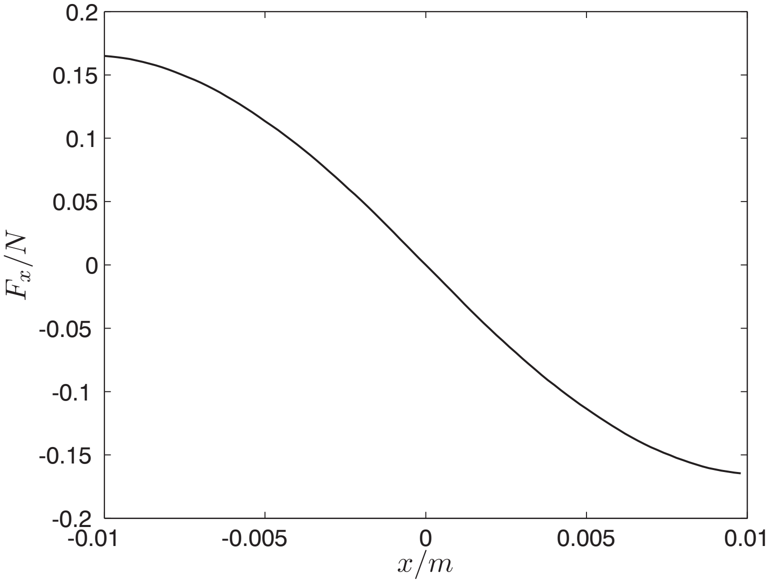

Figure 5.9: *Calculated force in x-direction F_x versus displacement x.*

The simulation time step is taken $\Delta t = 1$ ms, and the initial displacement of the armature in the x direction is $x_0 = 4$ mm.

The oscillation envelope (Fig. 5.10) is calculated as

$$\tau = A - A\left(1 - exp^{-\frac{c}{2m}t}\right) \; ; \qquad (5.13)$$

where A is the initial amplitude of the signal, in this case equal with the initial displacement x_0, m is the mass of the moving armature, c is the damping constant and t is the time.

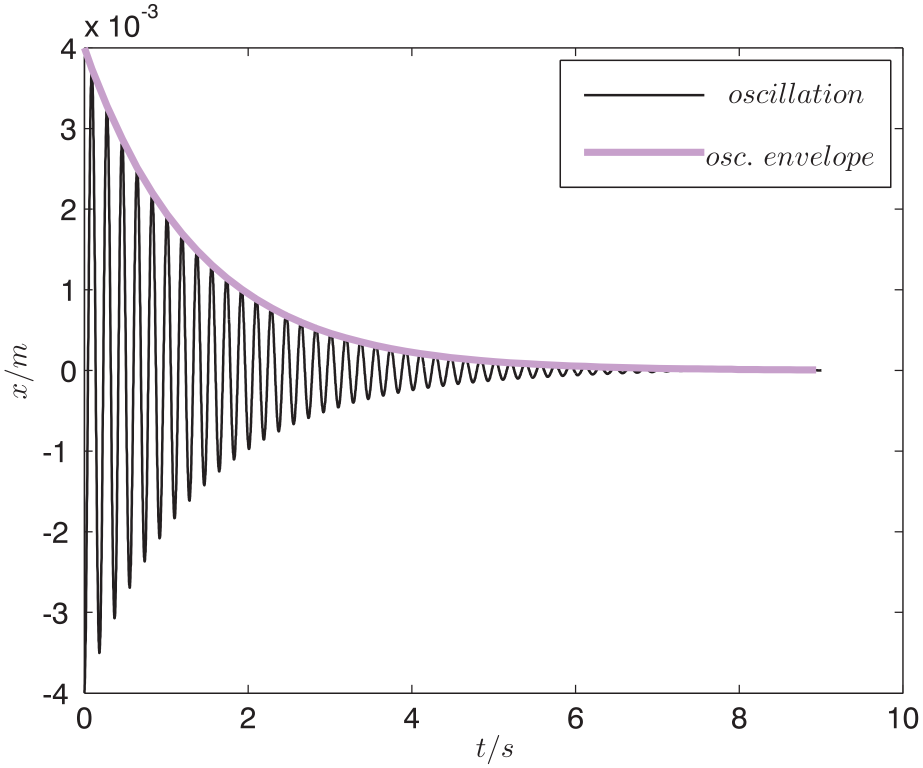

Figure 5.10: *Mechanical equation with damping: the oscillation of the moving armature in time and the oscillation envelope.*

5.3 Damping by Eddy Currents

Many electromagnetical devices contain parts that move in an electromagnetical field. Then, eddy currents are induced, which result in a damping of the mechanical system.

A transient simulation in the case of a 3D linear actuator, where the moving armature is displaced in x-direction, is performed. A coupled calculation, both considering a magnetic model and a mechanical model is carried out. When no damping or eddy-current effects are involved, a non-amortisated oscillation follows. If either damping or eddy currents are present, the oscillation will be damped until the equilibrium position is reached.

In the first case, the simulation is performed without any conductivity in the materials. Therefore, no eddy currents are induced, and the oscillation is non-amortisated. In Fig. 5.5 and Fig. 5.6, the results of a simulation with a time step $\Delta t = 5$ ms are presented.

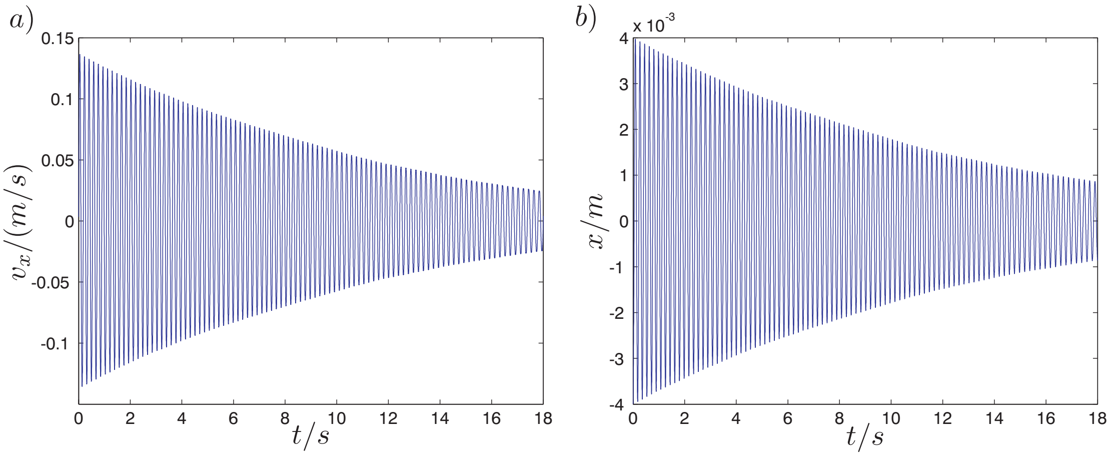

Figure 5.11: *a) Speed v_x and b) displacement in x-direction when the mobile armature has a conductivity of* $5e6$ *S/m.*

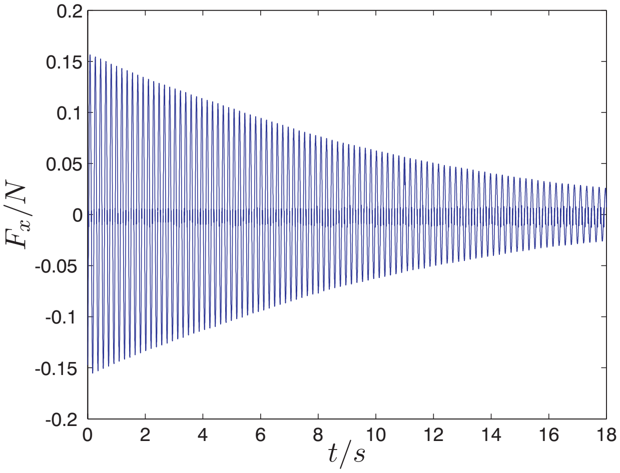

Figure 5.12: *Force in x-direction F_x when the mobile armature has a conductivity of* $5e6$ *S/m.*

Another simulation with a conductive moving armature is performed. For the moving armature, a conductive linear iron material with $\mu_r = 1000$ and a conductivity of $5e6$ S/m is used. Eddy currents are induced due to the movement. The moving armature is displaced initially with a value of $x = 4$ mm. Due to the magnetic field from the fixed armature, the moving armature is attracted, and the simulation can

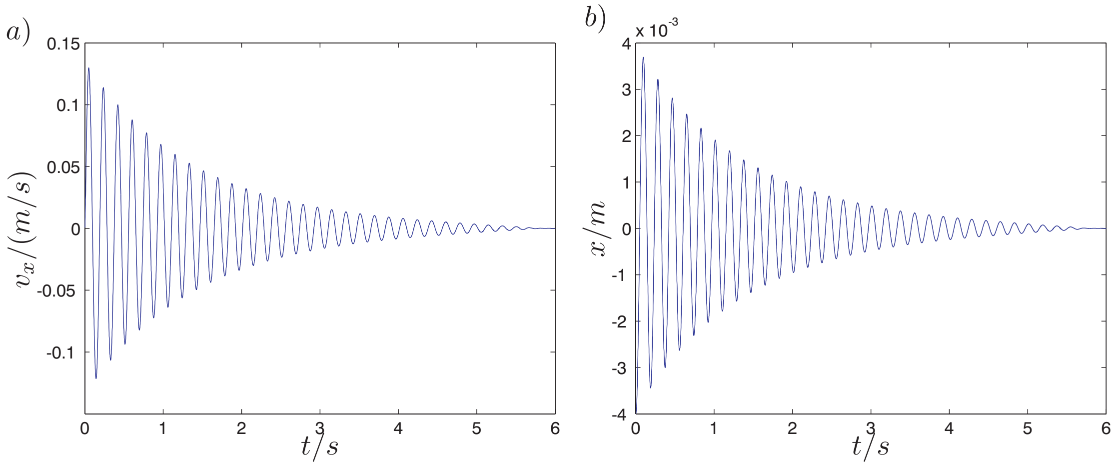

Figure 5.13: *a) Speed* v_x *and b) displacement in* x*-direction when the mobile armature has a conductivity of* $5e7$ *S/m.*

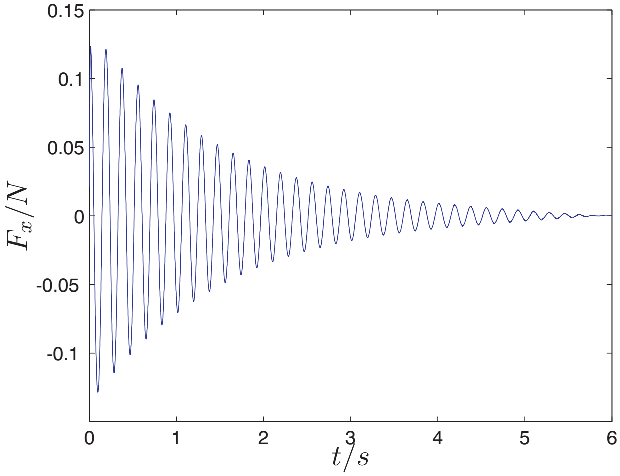

Figure 5.14: *Force in* x*-direction* F_x *when the mobile armature has a conductivity of* $5e7$ *S/m.*

be performed without initial speed. The induced eddy currents due to the movement decrease the force and the acceleration.

In Fig. 5.13 and Fig. 5.14, the results of a third simulation with a conductive mobile armature are presented. The material is also linear and the conductivity is $5e7$ S/m. It can be observed that for bigger values of eddy currents the force is decreasing quicker and the armature stops moving in about 6 s, for a simulation with a time step of 1 ms.

Chapter 6

Linear Actuator Example

The analysis of vibrations and the acoustic noise from electrical machines is very important. Due to magnetic forces, vibrations appear. In a not sufficiently stiff structure, these vibrations lead to acoustic noise [57], [58], [59].

6.1 Permanent Magnet Flux-Switching Machine

The studied linear actuator (Fig. 6.1) is developed and traded by PASIM Direktantriebe [7] and is used in industrial applications where fast and accurate linear positioning is required.

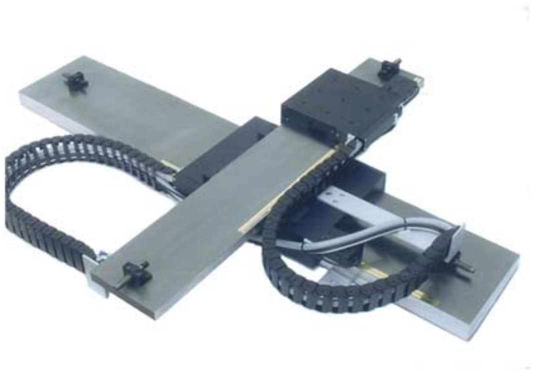

Figure 6.1: *Linear actuator - PASIM Direct drive.*

The construction data of the device are presented in Fig. 6.4. The length in the z-direction is 64 mm. The mobile armature is air-mounted on the fixed armature (rail). Both the moving and the fixed armature are toothed, and as a maintenance measure and as a protection against the dust, the teeth from the rail are filled with a polymer. The permanent magnet (PM) and the coils are incorporated into the moving armature: the PM has the relative permeability of $\mu_r = 1.1$, and the current flows through $N = 50$ copper coils with wires of 0.5 mm^2 area.

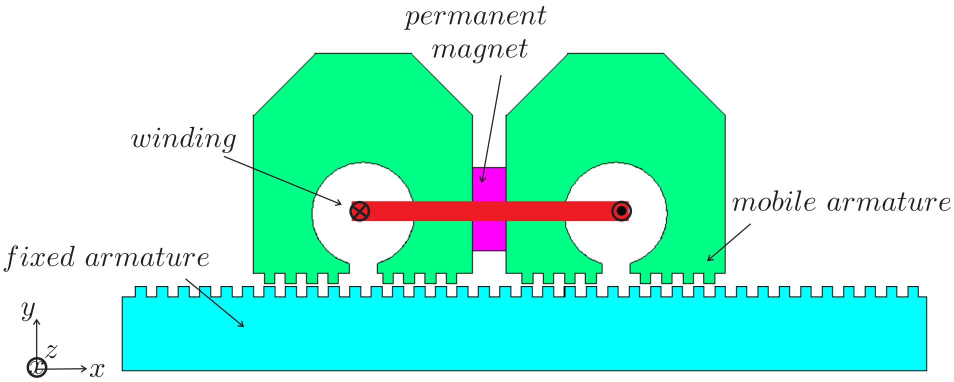

Figure 6.2: *Linear actuator - permanent magnet flux switching machine.*

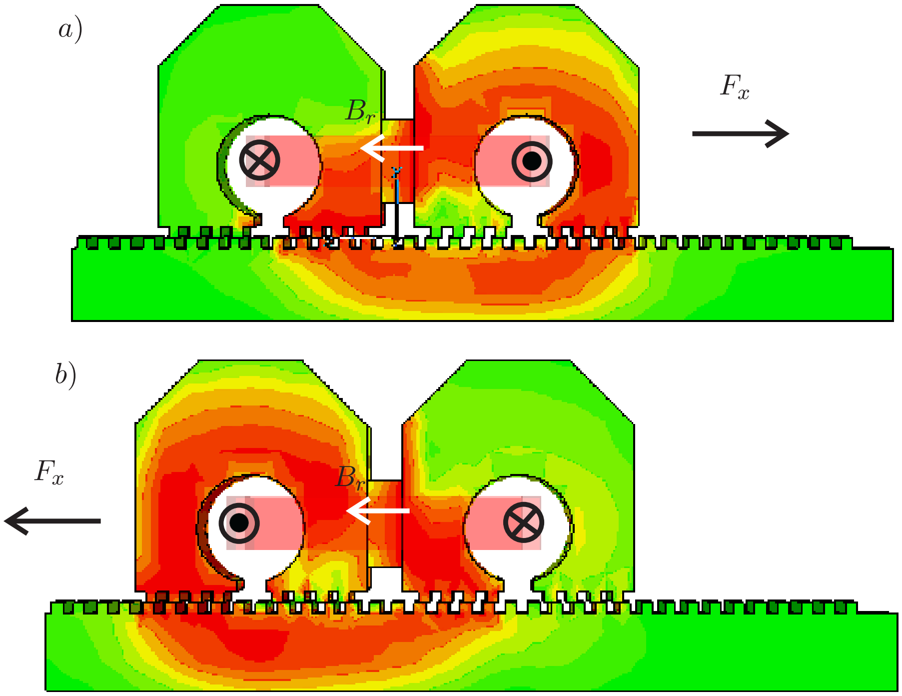

Figure 6.3: *Linear actuator - functioning principle.*

When it is supplied with a current in an adequate direction, the actuator is capable to produce a positive or a negative thrust. For the relative position of the armatures given in Fig. 6.3, a positive current will move the actuator in the right direction, whereas a negative current will move it in the left direction.

The force is obtained as it is graphically explained in Fig. 6.3 by superposition of the field by the PM and the field exerted by the coil. For example, in Fig. 6.3 a) the magnetic field has in the mobile armature a direction from right to left and the positive current cancels the field in the left sides of both half modules and in the same time increases the field in the right sides of the half modules.

The fixed and the moving part of the 3D linear actuator (Fig. 6.2) are discretized

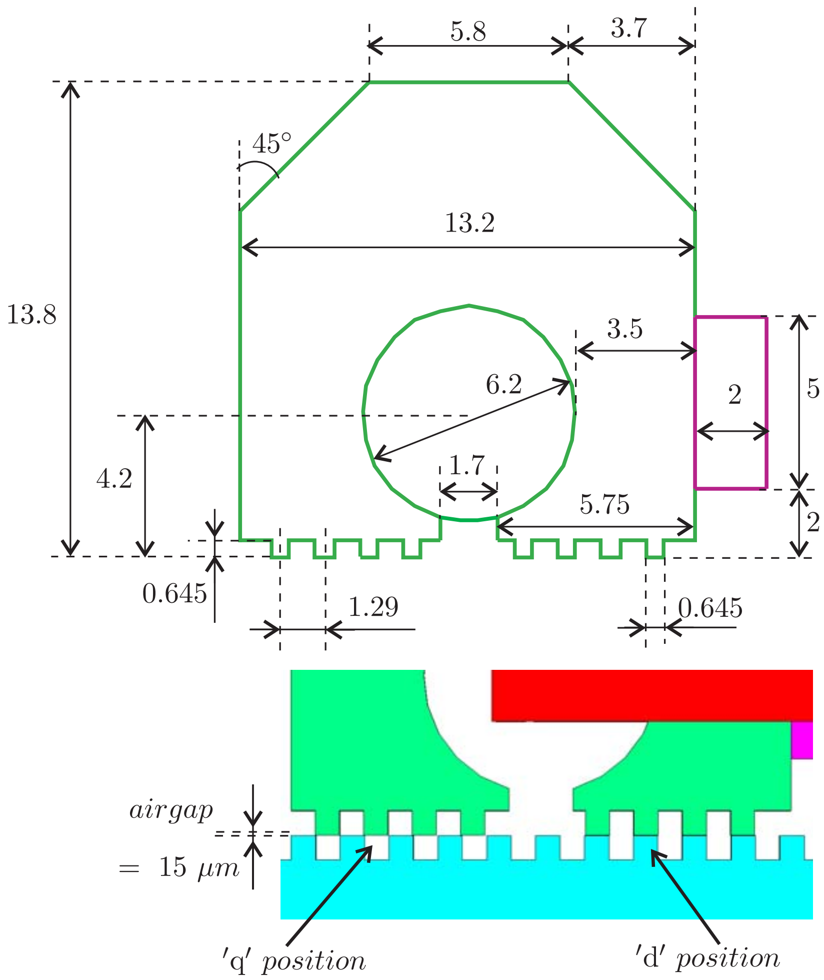

Figure 6.4: *Linear actuator - construction data (lengths in mm).*

independently by the Finite Integration Technique and are connected at a sliding surface situated in the air gap. The commercial package EM Studio for electromagnetic field simulation [31] is used to construct and to discretize the models. The rail is made from massive nonlinear iron with the conductivity of $1e7$ S/m, whereas the modules of the mobile armature are made from laminated iron. The dependence of the force on the relative position of the armatures is calculated. A tooth pitch consisting of a single tooth and a single slot of the rail is actually one period of the parameter variation.

The model in the z-direction (perpendicular to the cross-sectional plane of Fig. 6.2) is discretized by only one mesh cell. Consequently end-effects occurring within the real machine are not resolved by the FIT mesh. The solver is programmed as a module of DIDO (an in-house software package programmed in C++). This module allows the coupling of two meshes and the coupling of the magnetic model with a mechanical model. In this way it is possible to completely model the actuator's behavior by calculating the generated force and how the force is influenced by the relative position of the armatures. *The forces are calculated for two different geo-*

metrical arrangements in order to compare the differences in generated force and the produced vibrations.

6.2 Ferromagnetic Saturation

The nonlinear ferromagnetic material behavior can be expressed in two ways. The first modeling approach is:

$$\mathbf{B} = \mu_{\mathbf{0}}(\mathbf{H} + \mathbf{M}) \ , \tag{6.1}$$

where $\mathbf{M}$ is the magnetization that includes the information of the nonlinear material. The discrete formulation on the basis of the FIT reads:

$$\widehat{\widehat{\mathbf{b}}} = \mathbf{M}_{\mu_0}(\widehat{\mathbf{h}} + \widehat{\mathbf{m}}) \ , \tag{6.2}$$

where the vector $\widehat{\mathbf{m}}$ is defined on the dual edges and represents the magnetization. The second modeling approach uses a constitutive material relation between the magnetic field intensity $\mathbf{H}$ and magnetic induction $\mathbf{B}$:

$$\mathbf{B} = \mu\mathbf{H} \ , \tag{6.3}$$

where the permeability μ contains the information of the nonlinear material. For fields discretized by FIT, the above equation becomes:

$$\widehat{\mathbf{h}} = \mathbf{M}_{\nu}(\widehat{\widehat{\mathbf{b}}})\widehat{\widehat{\mathbf{b}}} \ , \tag{6.4}$$

where the reluctivity matrix $\mathbf{M}_\nu$ depends on the $H(B)$ curve of the ferromagnetic material. For this example the second modeling approach is used, with the $B - H$ curve from Fig. 6.5.

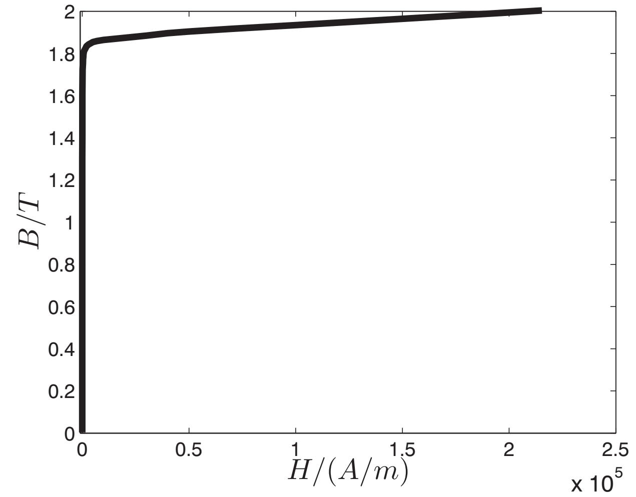

Figure 6.5: *B-H curve.*

Ferromagnetic saturation has a large influence on the device behavior and therefore has to be introduced into the simulation. In certain positions close to the unaligned position (*quadrature axis*-position), the field is concentrated into a very small corner giving rise to very high saturation.

For a magnetostatic problem with a ferromagnetic material with a nonlinear magnetization curve, the material matrix $\mathbf{M}_\nu$ depends on the unknown magnetic vector potential $\widehat{\mathbf{a}}$, resulting the nonlinear formulation [60]:

$$\widetilde{\mathbf{C}}\mathbf{M}_\nu(\widehat{\mathbf{a}}(t))\;\mathbf{C}\widehat{\mathbf{a}}(t)+\mathbf{M}_\kappa\frac{d}{dt}\widehat{\mathbf{a}}(t)=\widehat{\widehat{\mathbf{j}}}_s(t)+\widetilde{\mathbf{C}}\mathbf{M}_\nu(\widehat{\mathbf{a}}(t))\;\widehat{\widehat{\mathbf{b}}}_\mathrm{r}\;. \tag{6.5}$$

The iteration matrix is symmetric and positive definite. The linear system is solved using the Conjugate Gradient algorithm, preconditioned by the Symmetric Successive Over Relaxation (SSOR) method, which require a low memory and feature a superlinear convergence behavior. The nonlinear system of equations is solved by a sequence of linear algebraic equations using the Successive Approximation technique or the Newton method.

6.3 Nonlinear Transient Simulation

When the ferromagnetic materials have a nonlinear magnetization curve, the reluctivity material matrix $\mathbf{M}_\nu$ depends on the unknown vector potential: $\mathbf{M}_\nu = \mathbf{M}_\nu(\widehat{\mathbf{a}})$, resulting in the nonlinearity of formulation (6.5) [62]. Therefore, a suitable choice of implicit time integration is required. Combining the discrete material model (6.4) and the magnetoquasistatic FIT formulation, and applying Eq. (5.3) and (5.4) as temporal discretization by the *Theta-method*, one obtains:

$$\begin{aligned}\widetilde{\mathbf{C}}\mathbf{M}_\nu\mathbf{C}\;(\theta\widehat{\mathbf{a}}^{(n+1)}+(1-\theta)\widehat{\mathbf{a}}^{(n)})+\frac{\mathbf{M}_\kappa}{\Delta t}\;(\widehat{\mathbf{a}}^{(n+1)}-\widehat{\mathbf{a}}^{(n)})&\\ =\theta\widehat{\widehat{\mathbf{j}}}_\mathrm{s}^{(n+1)}+(1-\theta)\widehat{\widehat{\mathbf{j}}}_\mathrm{s}^{(n)}+\widetilde{\mathbf{C}}\mathbf{M}_\nu\widehat{\widehat{\mathbf{b}}}_\mathrm{r},&\end{aligned} \tag{6.6}$$

where the first given value is $\widehat{\mathbf{a}}_0 = \widehat{\mathbf{a}}(t_0)$ and the value at the new time step is $\widehat{\mathbf{a}}^{(n+1)} = \widehat{\mathbf{a}}(t^{(n)} + \Delta t)$.

Regarding that the moving and the fixed part of the linear actuator are coupled at a sliding surface, Eq. (6.6) becomes for the coupled system of equations:

$$\begin{aligned}&\begin{bmatrix}\mathbf{K}_\mathrm{fx} & 0\\ 0 & \mathbf{K}_\mathrm{mv}\end{bmatrix}\begin{bmatrix}\widehat{\mathbf{a}}_\mathrm{fx}^{(n+1)}\\ \widehat{\mathbf{a}}_\mathrm{mv}^{(n+1)}\end{bmatrix}+\begin{bmatrix}\mathbf{g}_\mathrm{fx}^{(n+1)}\\ \mathbf{g}_\mathrm{mv}^{(n+1)}\end{bmatrix}= \qquad (6.7)\\ &=\begin{bmatrix}\frac{\mathbf{M}_{\kappa,\mathrm{fx}}}{\Delta t} & 0\\ 0 & \frac{\mathbf{M}_{\kappa,\mathrm{mv}}}{\Delta t}\end{bmatrix}\begin{bmatrix}\widehat{\mathbf{a}}_\mathrm{fx}^{(n)}\\ \widehat{\mathbf{a}}_\mathrm{mv}^{(n)}\end{bmatrix}+\begin{bmatrix}0\\ \widehat{\widehat{\mathbf{j}}}_\mathrm{s,mv}\end{bmatrix}+\begin{bmatrix}0\\ \widetilde{\mathbf{C}}_\mathrm{mv}\mathbf{M}_{\nu,\mathrm{mv}}\widehat{\widehat{\mathbf{b}}}_\mathrm{r}\end{bmatrix},\end{aligned}$$

where

$$\mathbf{K}_{\mathrm{fx}} = \widetilde{\mathbf{C}}_{\mathrm{fx}}\mathbf{M}_{\nu,\mathrm{fx}}\mathbf{C}_{\mathrm{fx}} + \frac{\mathbf{M}_{\kappa,\mathrm{fx}}}{\Delta t}\ ; \tag{6.8}$$

$$\mathbf{K}_{\mathrm{mv}} = \widetilde{\mathbf{C}}_{\mathrm{mv}}\mathbf{M}_{\nu,\mathrm{mv}}\mathbf{C}_{\mathrm{mv}} + \frac{\mathbf{M}_{\kappa,\mathrm{mv}}}{\Delta t} \tag{6.9}$$

are the system matrices of the fixed and moving armatures, respectively. The integrated magnetic vector potentials $\widehat{\mathbf{a}}_{\mathrm{fx}}$ and $\widehat{\mathbf{a}}_{\mathrm{mv}}$ are the unknowns in the models, $\mathbf{M}_{\kappa,\mathrm{fx}}$ and $\mathbf{M}_{\kappa,\mathrm{mv}}$ are the conductivity matrices, $\widehat{\widehat{\mathbf{j}}}_{\mathrm{mv}}$ is the source current and $\widehat{\widehat{\mathbf{b}}}_{\mathrm{r}}$ is the integrated remanent flux density. The magnetic voltage $\mathbf{g}_{\mathrm{fx}}^{(n+1)}$ and $\mathbf{g}_{\mathrm{mv}}^{(n+1)}$ exerted from one model part upon the other are eliminated from the system as described in Chapter 3, Section 3.3.

6.3.1 Newton Scheme

A nonlinear system of equation can be solved by a sequence of linear algebraic problems using the Successive Approximation technique or the Newton method. The Newton method is faster than Successive Approximation technique, but none of these techniques is always stable when is applied to nonlinear materials.

The Newton method solves the nonlinear problem by solving a sequence of the linear problem by the same kind [63]. For example, a function:

$$F(x) = y^* \tag{6.10}$$

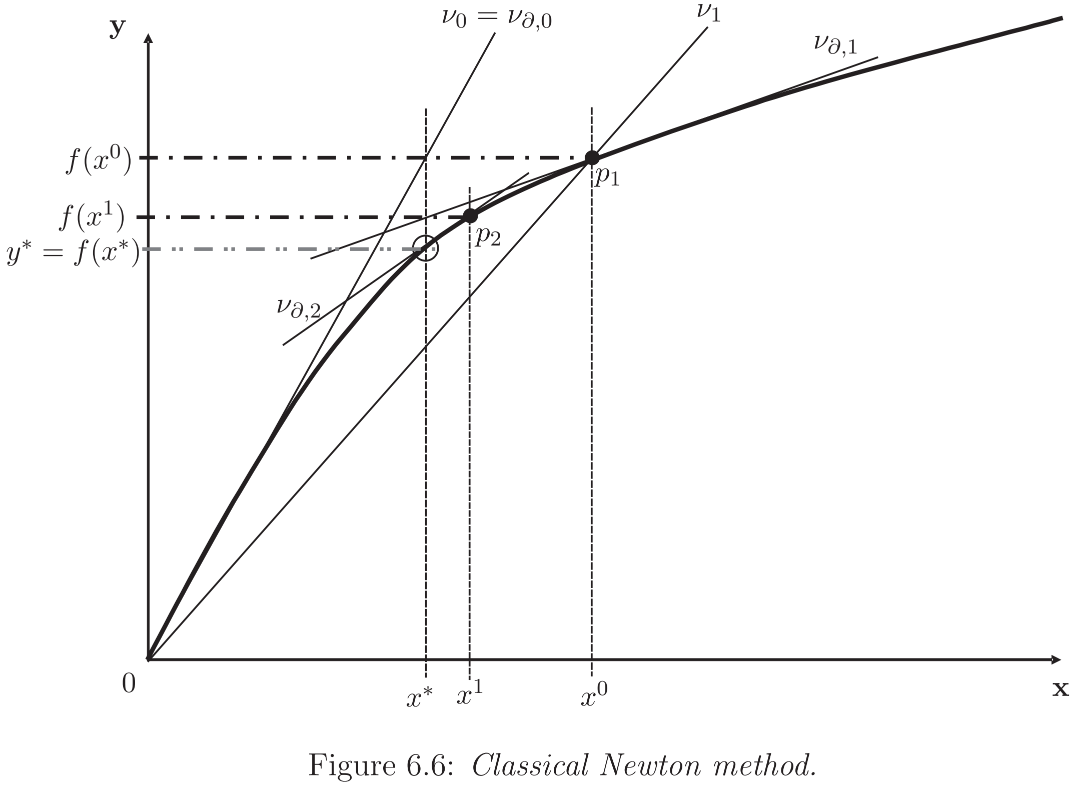

Figure 6.6: *Classical Newton method.*

is taken, where F is at least once continuously differentiable. If the starting guess is x^0 and the unknown solution is x^*, then the successive liniarization of Newton method reads:

$$F'(x^k)\ \Delta x^k = y^* - F(x^k), \quad x^{k+1} = x^k + \Delta x^k, \quad k = 0, 1, \ldots \ . \tag{6.11}$$

The Newton method has a quadratic convergence, that requires use of derivation of the non-linear function F. The procedure can be unstable near a horizontal asymptote or a local extremum, so a good choice of a starting guess x^0 is necessary.

The reluctivity matrix $\mathbf{M}_\nu$ is created in FIT by $\mathbf{M}_\nu = \widetilde{\mathbf{D}}_S \mathbf{D}_\nu \mathbf{D}_A^{-1}$ (see Eq. (2.52)), where $\widetilde{\mathbf{D}}_S$ is the diagonal matrix of the length of the dual edges, $\mathbf{D}_A$ is the diagonal matrix of the areas of the primary facets and $\mathbf{D}_\nu$ is a diagonal matrix of reluctivities. The uni-directional Newton technique [64] is used to ensure a rapid convergence (see Fig. 6.7). The new differential reluctivity used is:

$$\nu_d = \nu + \frac{\partial \nu}{\partial \mid B \mid} \mid B \mid \ . \tag{6.12}$$

The new differential material parameter is applied on the normal grid G and is calculated exactly as the normal parameter $\mathbf{D}_\nu$: $\mathbf{D}_{\nu_d} = \mathrm{diag}\{\nu_\mathrm{i}\}$. A new material matrix is constructed on the basis of ν_d: $\mathbf{M}_{\nu_d} = \mathbf{D}_{\widetilde{S}} \mathbf{D}_{\nu_d} \mathbf{D}_A^{-1}$.

Since the permeability ν depends on the local magnetic flux density, a nonlinear equation system has to be solved at each time step. The magnetoquasistatic system

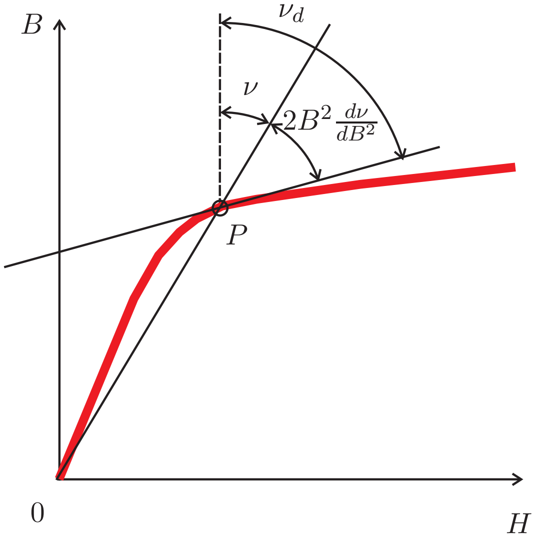

Figure 6.7: *Uni-directional Newton method.*

equation changes to:

$$\begin{aligned}
&\begin{bmatrix} \widetilde{\mathbf{C}}_{\mathrm{fx}}\mathbf{M}_{\nu_d,\mathrm{fx}}\mathbf{C}_{\mathrm{fx}} + \frac{\mathbf{M}_{\kappa,\mathrm{fx}}}{\Delta t} & 0 \\ 0 & \widetilde{\mathbf{C}}_{\mathrm{mv}}\mathbf{M}_{\nu_d,\mathrm{mv}}\mathbf{C}_{\mathrm{mv}} + \frac{\mathbf{M}_{\kappa,\mathrm{mv}}}{\Delta t} \end{bmatrix} \begin{bmatrix} \mathbf{p}_{\mathrm{fx}}^{(n+1),(k+1)} \\ \mathbf{p}_{\mathrm{mv}}^{(n+1),(k+1)} \end{bmatrix} + \begin{bmatrix} \mathbf{g}_{\mathrm{fx}}^{(n+1)(k+1)} \\ \mathbf{g}_{\mathrm{mv}}^{(n+1)(k+1)} \end{bmatrix} \\
&\quad = \begin{bmatrix} \widetilde{\mathbf{C}}_{\mathrm{fx}}\mathbf{M}_{\nu,\mathrm{fx}}\mathbf{C}_{\mathrm{fx}} + \frac{\mathbf{M}_{\kappa,\mathrm{fx}}}{\Delta t} & 0 \\ 0 & \widetilde{\mathbf{C}}_{\mathrm{mv}}\mathbf{M}_{\nu,\mathrm{mv}}\mathbf{C}_{\mathrm{mv}} + \frac{\mathbf{M}_{\kappa,\mathrm{mv}}}{\Delta t} \end{bmatrix} \begin{bmatrix} \widehat{\mathbf{a}}_{\mathrm{fx}}^{(n+1),(k)} \\ \widehat{\mathbf{a}}_{\mathrm{mv}}^{(n+1),(k)} \end{bmatrix} - \\
&\quad - \begin{bmatrix} \frac{\mathbf{M}_{\kappa,\mathrm{fx}}}{\Delta t} & 0 \\ 0 & \frac{\mathbf{M}_{\kappa,\mathrm{mv}}}{\Delta t} \end{bmatrix} \begin{bmatrix} \widehat{\mathbf{a}}_{\mathrm{fx}}^{(n)} \\ \widehat{\mathbf{a}}_{\mathrm{mv}}^{(n)} \end{bmatrix} - \begin{bmatrix} 0 \\ \widehat{\widehat{\mathbf{j}}}_{\mathrm{mv}} \end{bmatrix} - \begin{bmatrix} 0 \\ \widetilde{\mathbf{C}}_{\mathrm{mv}}\mathbf{M}_{\nu,\mathrm{mv}}\widehat{\widehat{\mathbf{b}}}_{\mathrm{r}} \end{bmatrix},
\end{aligned} \tag{6.13}$$

where superscript (n) is for transient iteration, (k) is for nonlinear iteration and term $\mathbf{p}$ is the solution's change. The solution $\widehat{\mathbf{a}}$ at iteration $(k+1)$ reads:

$$\widehat{\mathbf{a}}_{\mathrm{fx}}^{(n+1),(k+1)} = \widehat{\mathbf{a}}_{\mathrm{fx}}^{(n+1),(k)} - \mathbf{p}_{\mathrm{fx}}^{(n+1),(k+1)}. \tag{6.14}$$

The Newton iteration cycle invoked at each time step (n) is written in Table (6.1). The uni-directional Newton method features a quadratic convergence, but only in the vicinity of the solution. Several relaxation methods have been implemented in order to achieve global convergence and to improve the speed of convergence. For the linearization of the nonlinear problems, the vector $\widehat{\mathbf{a}}$ related to the magnetic vector potential is taken as the main unknown. A relaxation factor α_N is introduced to obtain $\widehat{\mathbf{a}}_{i+1}$ in the next calculation cycle:

$$\widehat{\mathbf{a}}^{(k+1)} = \widehat{\mathbf{a}}^{(k)} - \alpha_N\ \mathbf{p}^{(k+1)}. \tag{6.15}$$

Table 6.1: *Newton algorithm for the* (n)*th time step and* (k)*th nonlinear iteration of the exemplary decoupled system.*

```
1. Solve $\widehat{\mathbf{a}}^{(n+1),(k=0)}$ from $(\widetilde{\mathbf{C}}\mathbf{M}_\nu\mathbf{C} + \frac{\mathbf{M}_\kappa}{\Delta t})\widehat{\mathbf{a}}^{(n+1),(k=0)} = \mathbf{f}^{(n)} + \frac{\mathbf{M}_\kappa}{\Delta t}\widehat{\mathbf{a}}^{(n)}$
2. Calculate $\widehat{\widehat{\mathbf{b}}}^{(n+1),(k=0)} = \mathbf{C}\widehat{\mathbf{a}}^{(n+1),(k=0)}$
3. Update $\mathbf{M}_\nu = f(\widehat{\widehat{\mathbf{b}}}^{(n+1),(k=0)})$
4. Calculate $\mathbf{M}_{\nu,\mathrm{d}} = g(\mathbf{M}_\nu)$ according to (6.12)
For $k = 1$ until convergence
  5. Calculate $\mathbf{r}^{(n+1),(k)} = \widetilde{\mathbf{C}}\mathbf{M}_\nu\mathbf{C}\widehat{\mathbf{a}}^{(n+1),(k-1)} - \mathbf{f}^{(n)} + \frac{\mathbf{M}_\kappa}{\Delta t}(\widehat{\mathbf{a}}^{(n+1),(k-1)} - \widehat{\mathbf{a}}^{(n)})$
  6. Solve $\mathbf{p}^{(n+1),(k)}$ from $(\widetilde{\mathbf{C}}\mathbf{M}_{\nu_d}\mathbf{C} + \frac{\mathbf{M}_\kappa}{\Delta t})\mathbf{p}^{(n+1),(k)} = -\mathbf{r}^{(n+1),(k)}$
  7. Calculate $\widehat{\mathbf{a}}^{(n+1),(k)} = \widehat{\mathbf{a}}^{(n+1),(k-1)} - \alpha_N\ \mathbf{p}^{(n+1),(k)}$
  8. Calculate $\widehat{\widehat{\mathbf{b}}}^{(n+1),(k)} = \mathbf{C}\widehat{\mathbf{a}}^{(n+1),(k)}$
  9. Update $\mathbf{M}_\nu = f(\widehat{\widehat{\mathbf{b}}}^{(n+1),(k)})$, $\mathbf{M}_{\nu_d} = g(\mathbf{M}_\nu)$ according to (6.12)
  10. Calculate $\mathbf{r}^{(n+1),(k+1)} = -\mathbf{f}^{(n)} + \widetilde{\mathbf{C}}\mathbf{M}_\nu\mathbf{C}\widehat{\mathbf{a}}^{(n+1),(k)} + \frac{\mathbf{M}_\kappa}{\Delta t}(\widehat{\mathbf{a}}^{(n+1),(k-1)} - \widehat{\mathbf{a}}^{(n)})$
  11. If $(\|\mathbf{r}^{(n+1),(k+1)}\| \ / \ \|\mathbf{f}^{(n+1)}\|) > \varepsilon$ the convergence, otherwise proceed with 5.
12. $\mathbf{f}^{(n+1)} = \mathbf{f}^{(n)}$
13. $\widehat{\mathbf{a}}^{(n+1),(k)} = \theta\widehat{\mathbf{a}}^{(n+1),(k)} + (1-\theta)\widehat{\mathbf{a}}^{(n),(k)}$
```

Several techniques exist to select an appropriate relaxation factor α_N at each iteration step, like *Heuristic relaxation method*, which directly adapts the relaxation parameter in the relaxation process, or *Brent's method*, which is based on a parabolic interpolation [45].

6.4 Actuator with Small Pole Pitch

A field simulation is carried out for a single-phase linear actuator consisting of a single module (Fig. 6.2). For a single-phase actuator, a stable and an instable equilibrium position is encountered for every excitation current.

A static characteristic - force versus position is calculated for the displacement over a single tooth pitch and for different excitations currents. The applied force F_x vanishes at a displacement of half a tooth pitch (Fig. 6.8). Hence, the mobile armature does not feature a self-starting capability. Applying a positive or a negative current to the actuator's winding, will displace the module left or right for the positions different than the equilibrium position. The combined effect of the permanent magnet and the excitation coil causes a force in direction of motion [65]. The variation of the force F_y versus position is presented in Fig. 6.9.

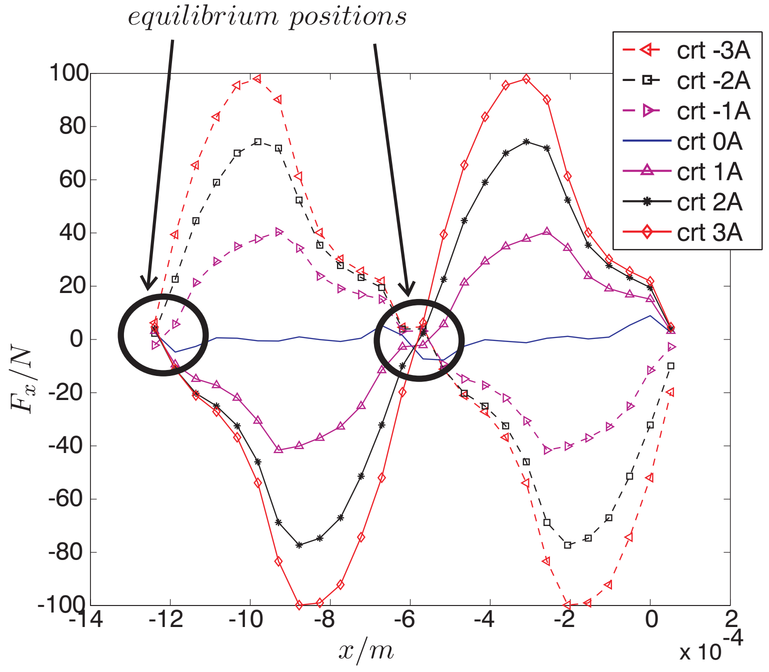

Figure 6.8: Force F_x versus position x.

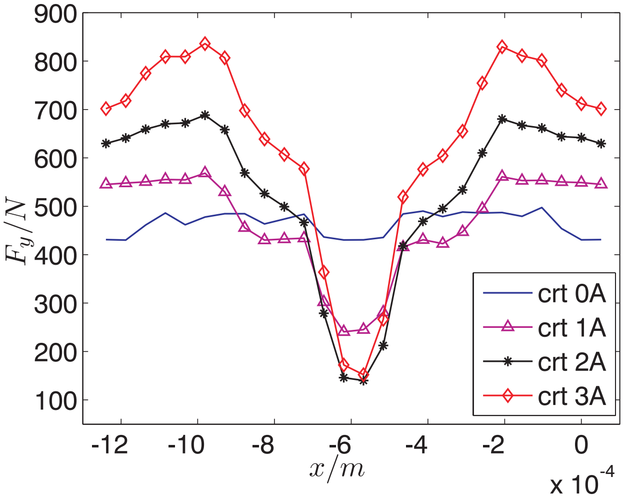

Figure 6.9: Force F_y versus position x.

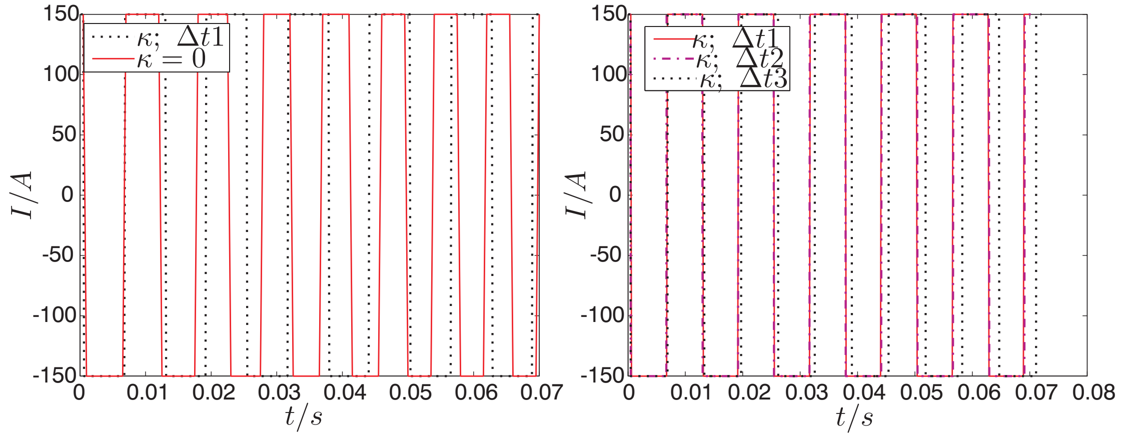

Figure 6.10: *Block current I for a model without conductivity* ($\kappa = 0$)*, and with conductivity* $\kappa = 1e7\ S/m$*, for time steps:* $\Delta t1 = 0.125\ ms$*,* $\Delta t2 = 0.0625\ ms$*,* $\Delta t3 = 0.03125\ ms$*.*

6.4.1 Single-Phase Configuration

For the numerical calculation, a linear actuator made from a single module is taken. In the case of a single module, the situation of an equilibrium position could be encountered. As can be seen in Fig. 6.8, at a displacement of 1/2 pole pitch, the applied force approximates zero, indicating that there is a chance that the mobile armature will not start moving. For this reason, an initial speed of 0.1 m/s is used for the simulation.

For coil excitation, an alternating block current with an amplitude of 3A, is used. The current is position controlled, such that it generates a positive force (Fig. 6.10).

Fig. 6.11 and Fig. 6.12 present the position versus time and the speed versus time in the case of a linear actuator with and without conductivity. The attraction force

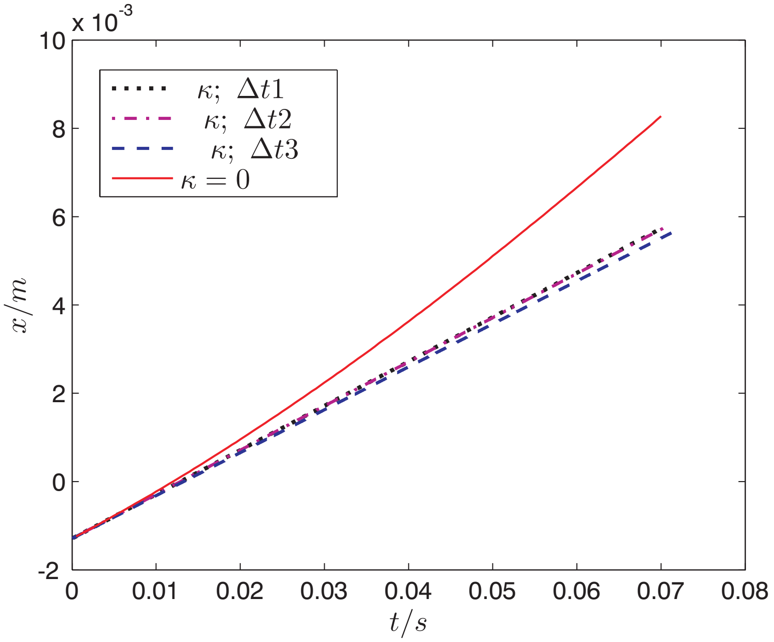

Figure 6.11: *Position x for a model without conductivity ($\kappa = 0$), and with conductivity $\kappa = 1e7$ S/m, for time steps: $\Delta t1 = 0.125$ ms, $\Delta t2 = 0.0625$ ms, $\Delta t3 = 0.03125$ ms.*

F_y in the case of a block current $I = [-3; 3]$ A and the displacement force F_x have smaller values in the case of a conductive material, as can be observed in Fig. 6.13 and Fig. 6.14. That reduces the acceleration correspondingly.

Fig. 6.11 and Fig. 6.12 present the position versus time and the speed versus time in the case of a linear actuator with and without conductivity, launched with an initial speed of 0.1 m/s.

6.4.2 Three-Phase Configuration

The 3-phase actuator (Fig. 6.15) consists of three modules. To ensure that the linear actuator will be able to start, each neighboring module is displaced by an integer number of tooth pitches plus a third part of a tooth pitch. The performance of the three-phase actuator is computed by a semi-analytical model using the static force-position characteristic (Fig. 6.8 and Fig. 6.9). The excitation currents of the different modules are dephased in time. In a first simulation, sinusoidal currents with an amplitude of $\hat{I} = 3$ A are applied (Fig. 6.16):

$$i_1 = \hat{I}\sin(\frac{x}{\tau_p}\,2\pi)\ , \tag{6.16}$$

$$i_2 = \hat{I}\sin(\frac{x+\frac{\tau_p}{3}}{\tau_p}\,2\pi)\ , \tag{6.17}$$

$$i_3 = \hat{I}\sin(\frac{x+\frac{2\tau_p}{3}}{\tau_p}\,2\pi)\ , \tag{6.18}$$

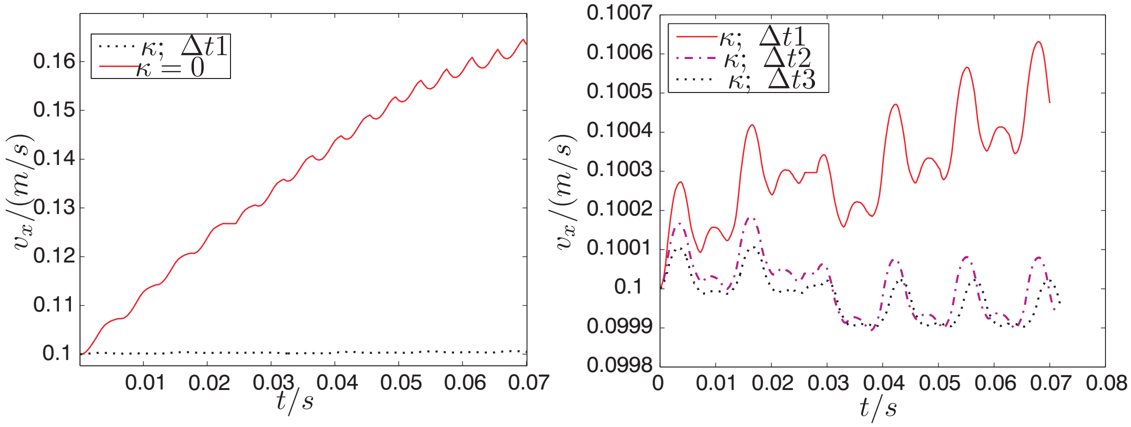

Figure 6.12: *Speed* v_x *for a model without conductivity* ($\kappa = 0$)*, and with conductivity* $\kappa = 1e7\ S/m$*, for time steps:* $\Delta t1 = 0.125\ ms$, $\Delta t2 = 0.0625\ ms$, $\Delta t3 = 0.03125\ ms$.

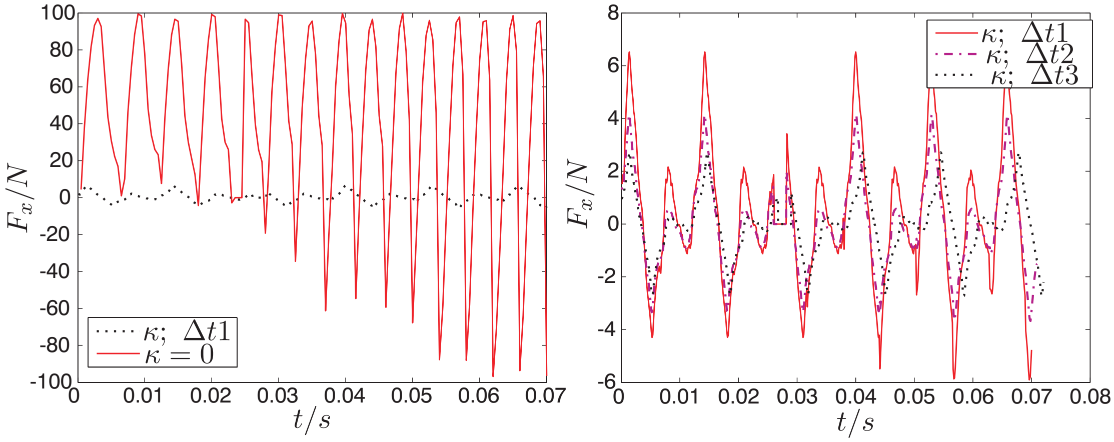

Figure 6.13: *Force* F_x *for a model without conductivity* ($\kappa = 0$)*, and with conductivity* $\kappa = 1e7\ S/m$*, for time steps:* $\Delta t1 = 0.125\ ms$, $\Delta t2 = 0.0625\ ms$, $\Delta t3 = 0.03125\ ms$.

In Eq. (6.16) - (6.18) the currents are directly expressed in terms of the relative positions of the armatures. This reflects the synchronous nature of the current excitation where the time variation of the currents is linked to the actuator's speed, i.e., $x = v_x\, t$.

The forces for all three modules are derived from the static force-position characteristic by:

$$F_{x1} = F_x(x, i_1)\ , \tag{6.19}$$

$$F_{x2} = F_x(x + \frac{\tau_p}{3}, i_2)\ , \tag{6.20}$$

$$F_{x3} = F_x(x + \frac{2\tau_p}{3}, i_3)\ , \tag{6.21}$$

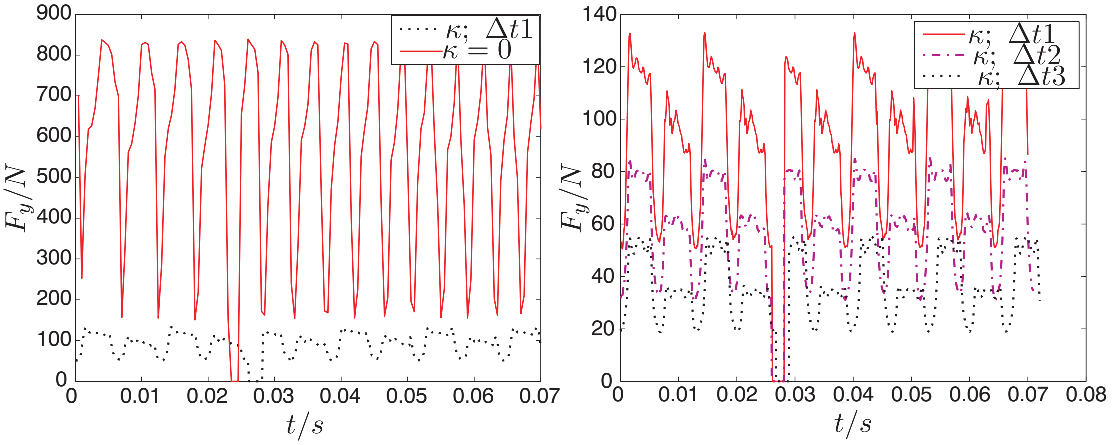

Figure 6.14: *Force F_y for a model without conductivity ($\kappa = 0$), and with conductivity $\kappa = 1e7$ S/m, for time steps: $\Delta t1 = 0.125$ ms, $\Delta t2 = 0.0625$ ms, $\Delta t3 = 0.03125$ ms.*

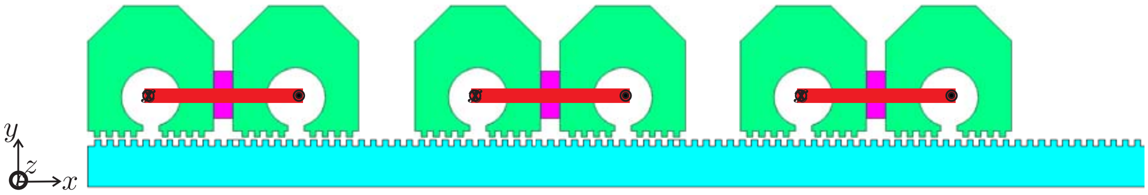

Figure 6.15: A 3-phased linear actuator: each module is displaced with $n + 1/3$ pole pitch.

and the total force is the sum of the all three forces:

$$F_x = F_{x1} + F_{x2} + F_{x3}. \tag{6.22}$$

The 3-phase actuator is simulated by combining the mechanical Eq. (5.10), the expressions (6.16) - (6.21) and the static force-position characteristic, organized as a look-up table. The cascaded simulation approach applied to the 3-phase actuator neglects eddy-current effects in the rail. The results for the thrust force are presented in Fig. 6.16 b). The increasing frequency of the excitation current is visible in Fig. 6.16 a).

In a second simulation, a controlled block current of $I = 3$ A is applied (Fig. 6.17):

$$i_1 = \begin{cases} -I & \text{if } x < \frac{\tau_p}{2} \\ I & \text{else} \end{cases}, \tag{6.23}$$

$$i_2 = \begin{cases} -I & \text{if } x + \frac{\tau_p}{3} < \frac{\tau_p}{2} \\ I & \text{else} \end{cases}, \tag{6.24}$$

$$i_3 = \begin{cases} -I & \text{if } x + \frac{2\tau_p}{3} < \frac{\tau_p}{2} \\ I & \text{else} \end{cases}. \tag{6.25}$$

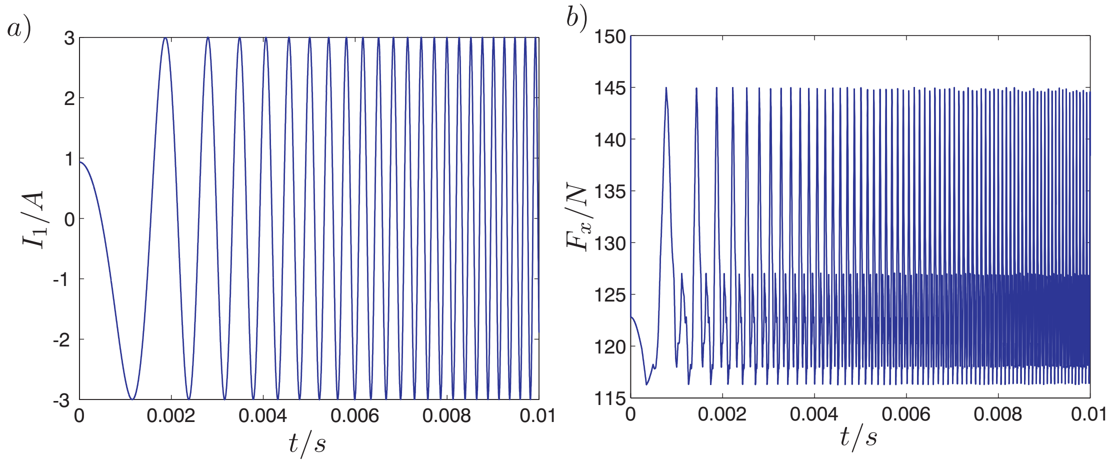

Figure 6.16: *First phase sinusoidal current I and the resulting total force* F_x.

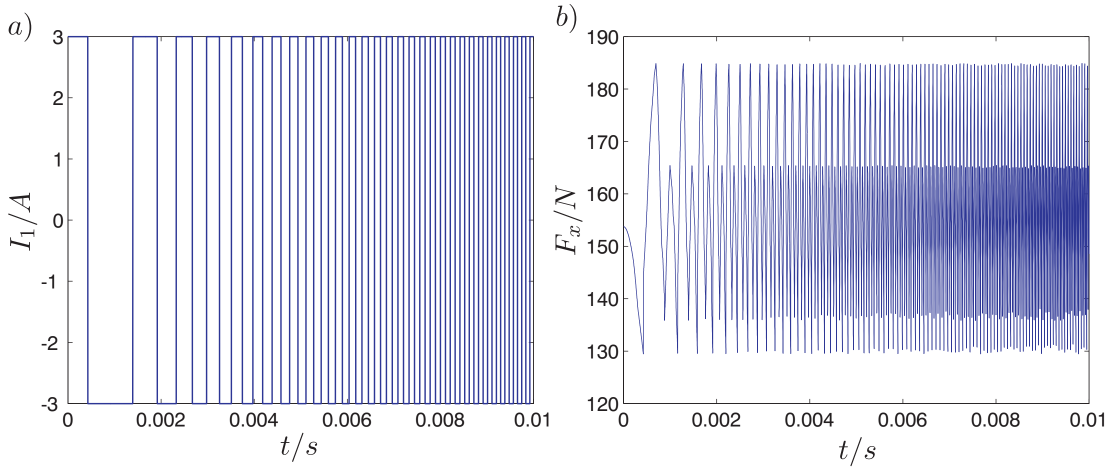

Figure 6.17: *First phase block current I and the resulting total force* F_x.

The control used was relatively primitive so the total force (Fig. 6.17 b)) shows high oscillations. The sinusoidal current gives a lower amplitude of the force than the one obtained with step currents, but exhibits lower oscillations. It is therefore possible with an adequate control to reduce the oscillations in the thrust force.

6.5 Actuator with Large Pole Pitch

During the movement of the linear actuator, transient vibration appear due to the magnetic forces. Acoustic noise is a result of these vibrations [57], [58]. A second configuration is tested in order to lower the noise from the audible spectrum. One module of the flux switching permanent magnet is shown in Fig. 6.18 and the construction data are presented in Fig. 6.19.

A static characteristic - force as a function of position for different (constant) current

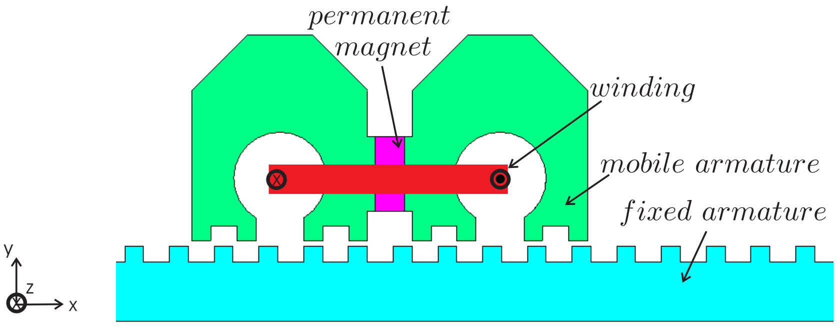

Figure 6.18: *2nd teeth configuration of the permanent magnet flux switching machine.*

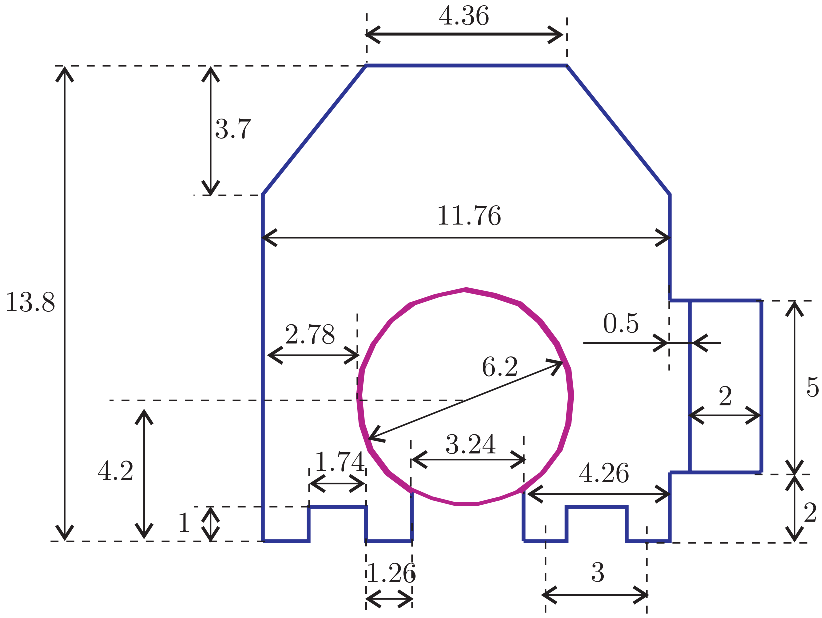

Figure 6.19: *Linear actuator - construction data for the second geometry (lengths in mm).*

excitation is calculated (Fig. 6.20 and Fig. 6.21). The equilibrium point corresponds to a displacement by half a pole pitch.

Even if the applied current is zero, the attraction force between the moving armature and the rail is different from zero, due to the permanent magnet present on the moving part.

6.5.1 Single-Phase Configuration

For the numerical calculation, a linear actuator made from a single module (Fig. 6.18) is taken. In the case of a single module, an equilibrium position can be encountered. As can be seen in Fig. 6.20, at a displacement of 1/2 tooth pitch, the applied force approximates zero, and there is a chance that the mobile armature

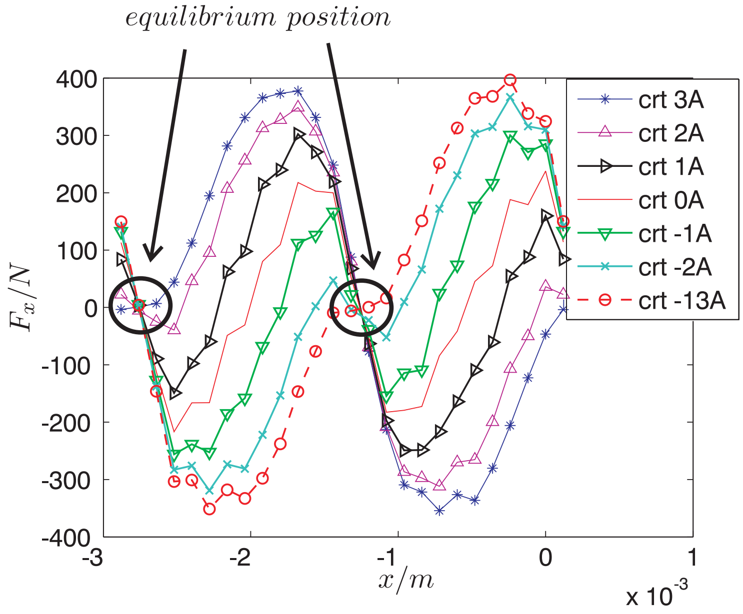

Figure 6.20: Force F_x versus position x.

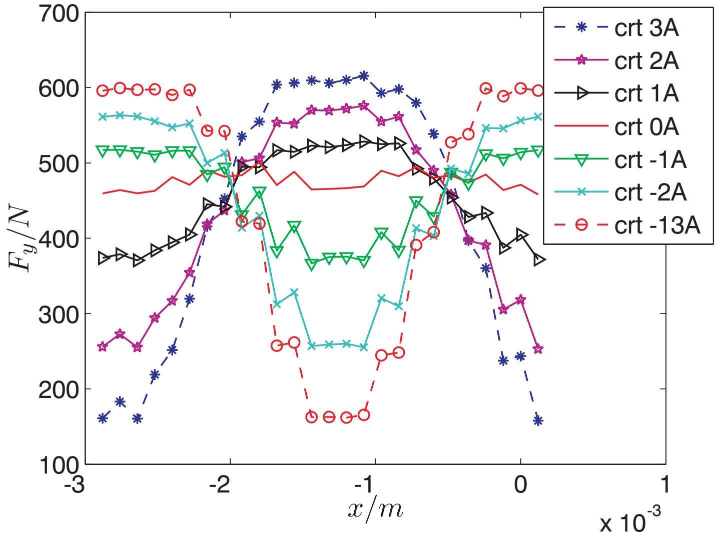

Figure 6.21: Force F_y versus position x.

will not start moving. The permanent magnets magnetically prestress the magnetic circuit in a certain direction. Hence, except for the situation of the equilibrium positions (Fig. 6.20), applying a positive or a negative current to the actuator's winding, will displace the module to the left or to the right. To be sure that the actuator will start, an initial speed of 0.1 m/s is used for the simulation, similar with the first small pole-pitch case.

The linear actuator was simulated with and without conductive material. When the moving armature has conductive iron, the simulation is made for different time steps in order to see the influence of the time step size on the calculations. Fig. 6.22

and Fig. 6.23 present the position versus time and the speed versus time. It can be seen that the speed in the presence of eddy currents is decreased.

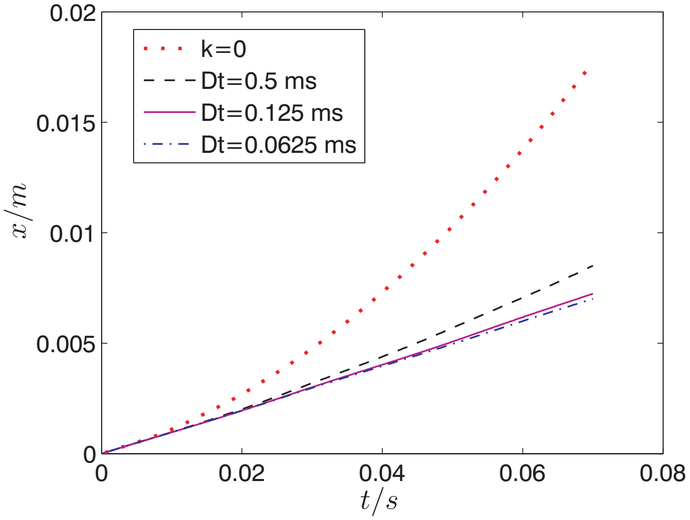

Figure 6.22: *Position x for a model without conductivity ($\kappa = 0$), and with conductivity $\kappa = 1e7$ S/m, for time steps: $\Delta t = 0.5$ ms, $\Delta t = 0.125$ ms, $\Delta t = 0.0625$ ms.*

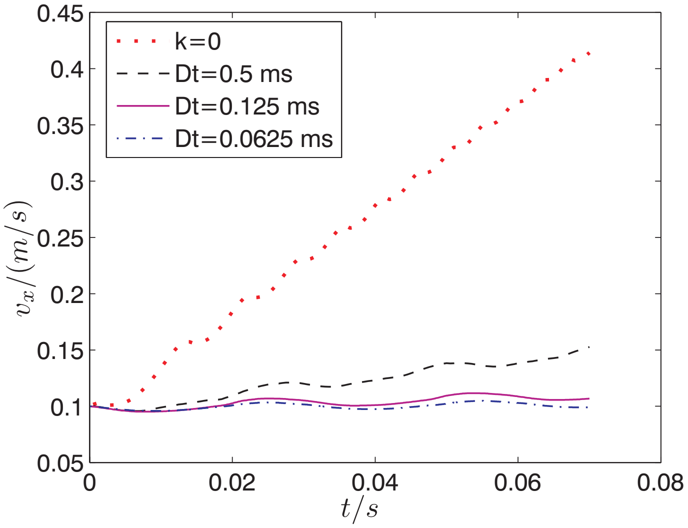

Figure 6.23: *Speed v_x for a model without conductivity ($\kappa = 0$), and with conductivity $\kappa = 1e7$ S/m, for time steps: $\Delta t = 0.5$ ms, $\Delta t = 0.125$ ms, $\Delta t = 0.0625$ ms.*

The attraction force F_y in the case of an alternating block current $I = [-3; 3]$ A and the displacement force F_x have smaller values in the case of a conductive material, as can be observed in Fig. 6.24 and Fig. 6.25.

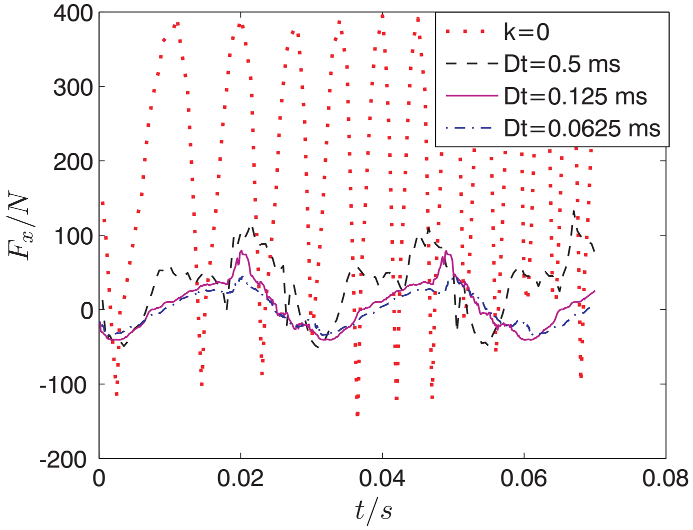

Figure 6.24: *Force F_x for a model without conductivity ($\kappa = 0$), and with conductivity $\kappa = 1e7\ S/m$, for time steps: $\Delta t = 0.5\ ms$, $\Delta t = 0.125\ ms$, $\Delta t = 0.0625\ ms$.*

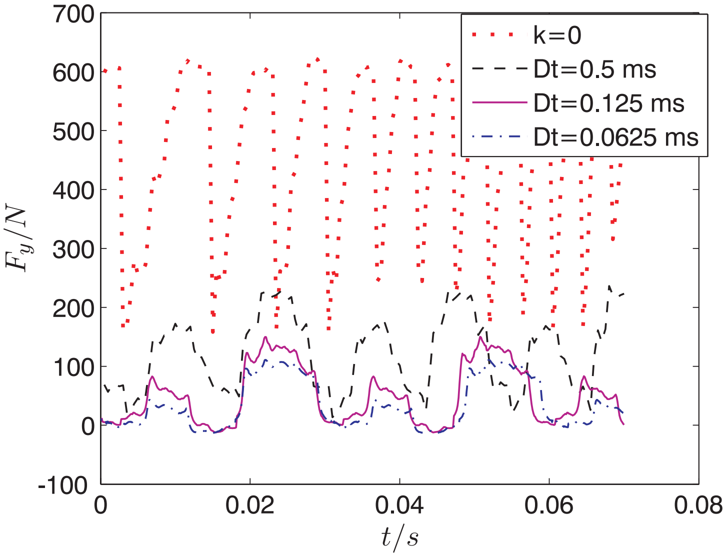

Figure 6.25: *Force F_y for a model without conductivity ($\kappa = 0$), and with conductivity $\kappa = 1e7\ S/m$, for time steps: $\Delta t = 0.5\ ms$, $\Delta t = 0.125\ ms$, $\Delta t = 0.0625\ ms$.*

6.5.2 Three-Phase Configuration

For the 3-phase actuator three modules are used, each neighboring module displaced by an integer number of pole pitches plus a third part of a pole pitch. A semi-analytical model is constructed using the static force-position characteristic. The excitation currents of the different modules are dephased in time.

The first case of simulation uses sinusoidal currents with an amplitude of $\hat{I} = 3$ A, using Eq. (6.16) - (6.18) (see Fig. 6.27).

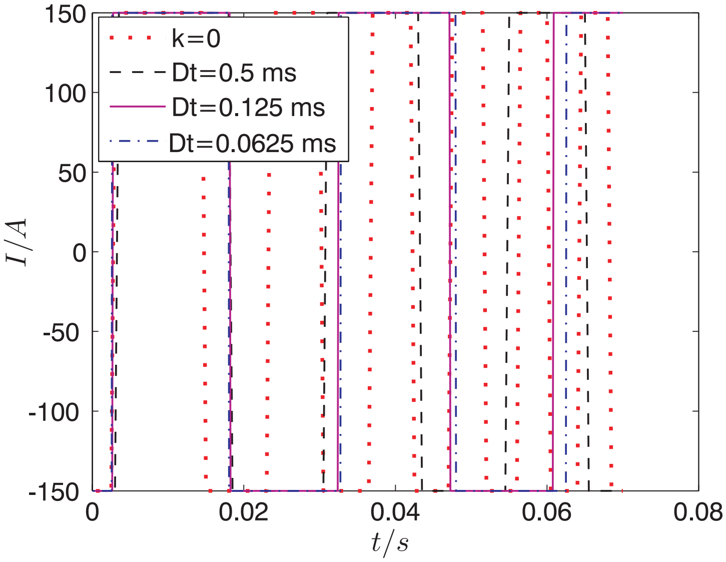

Figure 6.26: *Block current I for a model without conductivity ($\kappa = 0$), and with conductivity $\kappa = 1e7$ S/m, for time steps: $\Delta t = 0.5$ ms, $\Delta t = 0.125$ ms, $\Delta t = 0.0625$ ms.*

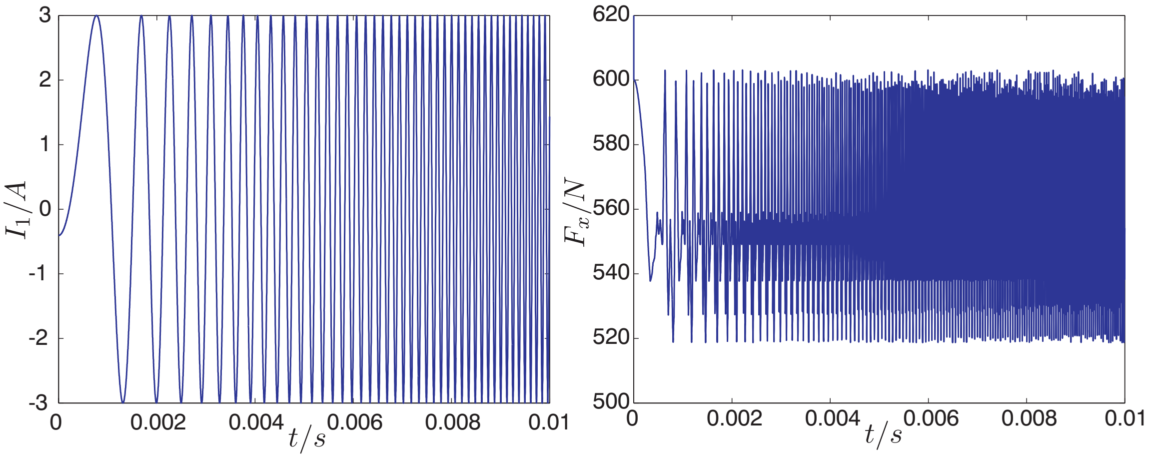

Figure 6.27: *First phase sinusoidal current I and the resulted total force F_x.*

The time variation of the currents is linked to the actuator's speed by $x = v_x\ t$. In Eq. (6.16) - (6.18), the currents are directly expressed in terms of the relative displacement of the armatures.

In the second set of simulations, a controlled block current of $I = [-3 : 3]$ A is applied (Fig. 6.28):

$$i_1 = \begin{cases} -I & \text{if } x < \frac{\tau_p}{2} \\ I & \text{else} \end{cases}, \tag{6.26}$$

$$i_2 = \begin{cases} -I & \text{if } x + \frac{\tau_p}{3} < \frac{\tau_p}{2} \\ I & \text{else} \end{cases}, \tag{6.27}$$

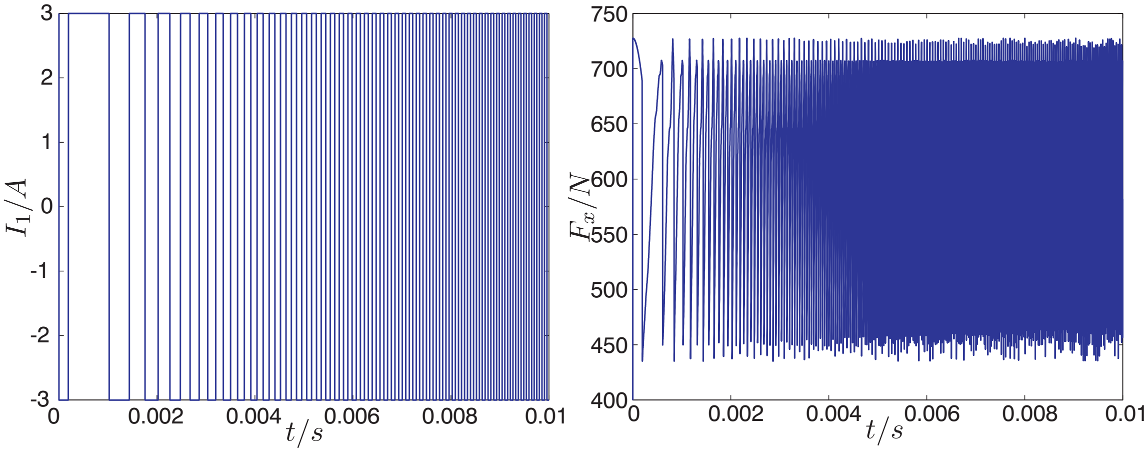

Figure 6.28: *First phase block current I and the resulted total force* F_x*.*

$$i_3 = \begin{cases} -I & \text{if } x + \frac{2\tau_p}{3} < \frac{\tau_p}{2} \\ I & \text{else} \end{cases} . \tag{6.28}$$

The forces for all three modules, for both excitation - with sinusoidal current or with block current are derived from the static force-position characteristic by:

$$F_{x1} = F_x(x, i_1) \ , \tag{6.29}$$

$$F_{x2} = F_x(x + \frac{\tau_p}{3}, i_2) \ , \tag{6.30}$$

$$F_{x3} = F_x(x + \frac{2\tau_p}{3}, i_3) \ , \tag{6.31}$$

$$F_{x,\text{total}} = F_{x1} + F_{x2} + F_{x3}. \tag{6.32}$$

The 3-phase actuator is simulated by combining the mechanical Eq. (5.10), the current expressions (6.16) - (6.18), the force expressions (6.29) - (6.31) and the static force-position characteristic, organized as a look-up table. The cascaded simulation approach applied to the 3-phase actuator neglects eddy-current effects in the rail.

The sinusoidal current gives a lower amplitude of the force than the force obtained with step currents. The second model has a better control than the first geometrical model.

The oscillation frequency of the forces for the second configuration with wide teeth is half of the frequency of the first configuration for the same speed.

Chapter 7

Summary, Conclusions and Outlook

This thesis deals with the transient 3D field simulation of electrical machines and actuators. The relative motion of the stator and rotor model parts is considered at a common interface in the air gap. The thesis compares different techniques for interpolating the degrees of freedom at both non-matching meshes constituting a sliding surface situated in the middle of the air gap. Each model part is separately discretised by the Finite Integration Technique (FIT). Two kinds of meshes are used: a circular mesh for a rotating permanent magnet synchronous machine and a Cartesian mesh for a linear actuator. For the linear actuator, a simulation with both a non-conductive and a conductive material, as well as for a linear and a non-linear iron is carried out.

Circular FIT Model, Permanent Magnet Synchronous Machine

A 6-pole permanent magnet synchronous machine is discretised by the FIT at a circular mesh. The stator and the rotor are independently discretised and then are coupled at a sliding surface. Three interpolation techniques for connecting both meshes (from the rotor and from the stator) are developed: the locked step approach, an approach with linear interpolation and an approach with trigonometric interpolation. The first one works only when the stator and the rotor meshes are equidistant along the direction of movement and are rotated over an integer number of grid cells. The other interpolation techniques allow for non-equidistant meshes and for displacements which can be fractional parts of a grid cell. The trigonometric interpolation uses fast Fourier transforms (FFTs), which gives better results in case of fractional displacements, but increases the computation time.

Cartesian FIT Model, Linear Actuator

A linear actuator is discretised by the FIT at a Cartesian mesh. The fixed and the moving armature are discretised independently and coupled afterwards at a sliding surface situated in the air gap. Because a movement in both x- and z-direction is possible, a 2D interpolation technique is necessary. Both the locked step and the linear interpolation techniques are implemented. The attraction forces between the moving and the fixed armature, as well as the displacement forces are calculated with the Maxwell stress tensor approach and with an approach using local analytical solutions evaluated by a FFT. Due to the fact that the vectors of magnetic field strength are allocated at different positions on the FIT grid, these values needs to be interpolated in order to calculate the force with the Maxwell stress tensor approach. The technique incorporating FFTs reduces the numerical error introduced by interpolation.

Transient Simulation, Linear Actuator

For the linear actuator, a simulation in time domain is performed. The first model considers the linear actuator with permanent magnets and linear iron. The mobile armature is displaced with an initial value x_0, and due to the excitation present on the fixed armature, the mobile armature oscillates along a plane parallel to the sliding surface. The kinetics of the actuator are modeled by a mechanical equation. When the system does not exhibit damping, a non-amortisated oscillation follows. Depending whether a large or a small value of the damping is present, the amortisation of the linear actuator's movement is fast or slow. If the moving armature is conductive, eddy currents are induced due to the movement. The eddy-current effect causes a decrease of the force and hence, introduce an electromagnetic damping effect. Therefore, the amplitude of the mobile armature's movement is decreasing.

Transient Simulation, Permanent Magnet Flux Switching Machine

The developed algorithms are applied for the transient simulation of a permanent magnet flux switching machine. The armatures are made from a non-linear laminated iron. The fixed armature (rail) and the moving armature are discretised independently and coupled by the linear interpolation technique at a sliding surface. The moving armature incorporates both a permanent magnet and a coil. As a consequence, an attraction force remains also when the coil is not excited.

Two different geometrical configuration models are simulated and evaluated. The force ripple is analyzed by the force calculation method based on the Maxwell stress tensor.

An actuator constructed from a single module is simulated in time domain, both without conductivity and with a conductivity of $1e7$ S/m. A force versus position characteristic is calculated for different constant current excitations. It is observed that at the beginning and at a half of a pole pitch, the force vanishes, which indicates the existence of two equilibrium points. When the actuator is positioned at the stabile equilibrium points, the actuator will not or hardly start by itself. Therefore, the simulations are performed with an initial speed. The iron is conductive. Therefore, eddy currents are induced, which decrease the force.

The 3-phase machine is constructed from 3 modules, where each neighboring module is displaced with a number of entire pole pairs plus 1/3 part of a pole pair. A semi-analytical model based on the single-phase force-versus-displacement characteristic is simulated. The device is either fed with a sinusoidal current or with an alternating block current.

The resulting forces contain high oscillations because the control was relatively primitive. From the simulation resulted that a controlled block input current yields larger forces but also introduces higher oscillations.

Conclusions

The coupling methods allow the use of two independent meshes for mobile and fixed armature within the simulation of an electrical machine. The technique is applicable when the air gap is circular or planar for a rotational or translational device respectively. Hence, the modeling of the movement of particular magnetic relays or plungers is not possible with this technique.

Although both meshes are independent, it is recommended that big differences in the grid resolution are avoided. This ensures that the interpolation error is acceptable and also that the FIT stiffness matrix structure is not significantly altered. The coupling by trigonometric interpolation leads to more accurate results than computed to the coupling by linear interpolation, but requires also substantially more computational time.

The force calculation is carried out at a surface in the middle of the air gap. The accuracy of the field values is improved by computing local analytical solutions relaying upon FFTs. The more accurate field values leads to better results for the forces.

The simulation of electromechanical system with body motion is possible, and mechanical and electromagnetical damping effect can be considered. The coupling techniques allow to calculate rotating and linear machines.

Outlook

The current implementation leads to transient 3D simulation that may lead to several weeks of computational time. Future research should address more efficient algebraic solution technique and parallel computing.

Resolving all relevant eddy-current effect requires the use of a very fine mesh. The impact of the corresponding high number of degrees of freedom can be lowered by the use of an adaptive mesh strategy, possibly allowing grid refinement and grid coarsening in between successive time steps.

Further improvements of the convergence speed by using different types of solvers will reduce the calculation effort.

Appendix A

Abbreviations

BC	Boundary Condition
DOF	Degree of Freedom
FEM	Finite Element Method
FIT	Finite Integration Technique
$\mathrm{FI}^2\mathrm{TD}$	Finite Integration Implicit Time Domain
MGE	Maxwell-Grid-Equations
MVP	Magnetic Vector Potential
PDE	Partial Differential Equation
PM	Permanent Magnet
PMSM	Permanent Magnet Synchronous Motors
JAC	Jacobi Method
GS	Gauss-Seidel Method
SSOR	Symmetric Successive Over-Relaxation Method
CG	Conjugate Gradients Method
MINRES	Minimal Residual Method

Appendix B

Applied Notations and Symbols

General Mathematical Symbols

$\mathbb{R}, \mathbb{C}$	Set of real, complex numbers	
$\vec{r}, \mathbf{r}$	Spatial vector	
$\vec{n}$	Versor of an area	
$\mathbf{M}, \mathbf{D}$	Matrix, diagonalmatrix	
$\mathbf{x}^T, \mathbf{M}^T$	Transpose of vector $\mathbf{x}$ and matrix $\mathbf{M}$	
$\mathbf{x}^H, \mathbf{M}^H$	Hermitian (complex conjugated transpose of) vector $\mathbf{x}$ and matrix $\mathbf{M}$	
$\mathbf{M}^{-1}$	Inverse matrix of $\mathbf{M}$	

Δt	Time step	s
f	Frequency	Hz
ω	Angular frequency	rad/s

$d\vec{s}$	Element of edge	m
$d\vec{A}$	Element of area	m^2
$d\vec{V}$	Element of volume	m^3
∂A	Boundary of the area A	
$\partial \Gamma$	Boundary of the domain Γ	
∂V	Boundary of the volume V	

Classical Continuous Field Theory

$\vec{E}$	Electric field strength	V/m ; N/C
$\vec{E}_\mathrm{n}$,$\vec{E}_\mathrm{t}$	Normal and tangential components of $\vec{E}$	V/m ; N/C
$\vec{D}$	Electric flux density (or electric induction)	C/m^2
$\vec{H}$	Magnetic field strength	A/m
$\vec{B}$	Magnetic flux density	T ; Vs/m^2
$\vec{J}_s$	Total (surface) current density	A/m^2
$\vec{J}_e$	External imposed current density	A/m^2
$\vec{J}_k$	Conduction current density	A/m^2
$\vec{J}_l$	Convection current density	A/m^2
$\vec{M}$	Magnetization	A/m
$\vec{M}_r$	Permanent magnetization	A/m
$\vec{J}_M$	Magnetic polarization	T
$\vec{P}$	Electrical polarization	C/m^2
$\vec{P}_r$	Permanent electrization	C/m^2
q,ρ	(Volume) charge density	C/m^3
c	Speed of light ($c = 299792458$m/s)	m/s
$\vec{A}$	Magnetic vector potential	Vs/m
$\vec{T}$	Electric vector potential	V
Ψ	Magnetic scalar potential	A
V	Electric scalar potential	V
μ	Scalar permeability	H/m
μ_0	Permeability of vacuum ($\mu_0 = 4\pi 10^{-7}$H/m)	H/m
μ_r	Relative permeability	
ε	Scalar permittivity	F/m; C^2/Jm
ε_0	Permittivity of free space ($\varepsilon_0 = 8.8541878176 \times 10^{-12}$F/m)	F/m ; C^2/Jm
ε_r	Relative permittivity	
κ (σ)	Scalar conductivity	S/m
χ	Scalar susceptibility	1
χ_e,χ_m	Electric and magnetic susceptibility	1
$\lambda_{thermal}$	Thermal conductivity	
$\vec{B}_r$	Remanence value of $\vec{B}$ (hysterezis loop)	T
$\vec{H}_c$	Coercive value of $\vec{H}$ (hysterezis loop)	A/m

Finite Integrations Technique

G,$\widetilde{G}$	Primary grid, dual grid	
N_p	Total number of nodes	
P,$\tilde{P}$	Primary grid nodes, dual grid nodes	
L,$\tilde{L}$	Primary / dual grid edges	m
A,$\tilde{A}$	Primary / dual grid facets	m^2
V,$\tilde{V}$	Primary / dual grid cell	m^3
$\Delta u_N, \Delta v_N, \Delta w_N$	Distance of grid nodes on the primary grid in Cartesian coordinates	m
$\Delta \tilde{u}_N, \Delta \tilde{v}_N, \Delta \tilde{w}_N$	Distance of grid nodes on the dual grid	m
$\Delta A_{uN}, \Delta A_{vN}, \Delta A_{wN}$	Distance of grid nodes on the primary grid	m^2
$\Delta r_N, \Delta \varphi_N, \Delta z_N$	Distance of grid nodes on the primary grid in cylindrical coordinates	m

$\widehat{\mathbf{e}}$	Vector of electric grid voltage	V
$\widehat{\mathbf{h}}$	Vector of magnetic grid voltage	A
$\widehat{\widehat{\mathbf{d}}}$	Vector of electric facet flux	C
$\widehat{\widehat{\mathbf{b}}}$	Vector of magnetic facet flux	Vs
$\widehat{\widehat{\mathbf{j}}}$	Vector of facet currents	A
$\widehat{\mathbf{a}}$	Vector of magnetic grid potential	Vs
$\widehat{\mathbf{m}}$	Vector of grid magnetization	A
$\widehat{\widehat{\mathbf{b}}}_\mathrm{r}$	Vector of grid remanence of permanent magnets	T
$\mathbf{C}, \widetilde{\mathbf{C}}$	Curl discrete operator on the primary/dual grid	
$\mathbf{S}, \widetilde{\mathbf{S}}$	Divergence discrete operator on the primary/dual grid	
$\mathbf{G}, \widetilde{\mathbf{G}}$	Gradient discrete operator on the primary/dual grid	
$\mathbf{M}_\varepsilon$	Material matrix of permittivity	F
$\mathbf{M}_\kappa$	Material matrix of conductivity	S
$\mathbf{M}_\mu$	Material matrix of permeability	H
$\mathbf{M}_\nu$	Material matrix of reluctivity	1/H
$\mathbf{M}_\rho$	Material matrix of resistivity	
$\mathbf{M}_{\nu_d}$	Material matrix of differential reluctivity	
$\mathbf{D}_A, \mathbf{D}_{\widetilde{A}}$	Diagonal matrix of primary/dual grid facets	
$\mathbf{D}_S, \mathbf{D}_{\widetilde{S}}$	Diagonal matrix of primary/dual grid edges	

Coupling

$\mathbf{P}$	Projector matrix
$\mathbf{Q}$	Selector matrix
$\mathbf{K}$	System matrix
γ	Periodicity of boundary condition
$\mathbf{k}_{\text{shift}}$	Shift operator
$\mathbf{k}_{\text{shift}}^{\text{positive}}$	Shift operator for periodic positive BCs
$\mathbf{k}_{\text{shift}}^{\text{negative}}$	Shift operator for periodic negative BCs
$\mathbf{k}_{\text{shift}}^{0}$	Shift operator for Dirichlet BCs
$\mathbf{k}_{\epsilon}$	Interpolation operator
$\mathbf{k}_{\text{trig}}$	Trigonometric operator
$\mathbf{R}_{\alpha}$	Diagonal rotation matrix

Circuit Theory

I_d	Direct current	A
I_q	Quadratic current	A
ϕ, α	Load angle	
N,N_t	Number of turns	
R, S, T	Phase angles	
L_{11}	Self inductance	H
W_{co}	Co-energy	J
F	Force	N
T	Electromagnetic torque	Nm
Ψ	Total flux linkage	Wb; V s
ϕ	Flux linkage	Wb; V s
e	Electromotive force	V
m	Mass	kg
c	Damping constant	
k	Spring constant	

Bibliography

[1] D. Rodger, H. Lai, P. Leonard, *Coupled Elements for Problems Involving Movement*, IEEE Trans. on Magn., Vol. 26, No. 2, pp. 548-550, March 1990.

[2] B. Davat, Z. Ren, and M. Lajoie-Mazenc, *The Movement in Field Modeling*, IEEE Trans. on Magn., Vol. 21, No. 6, pp. 2296 - 2298, Nov. 1985.

[3] I. Tsukerman, *Acurate Computation of 'Ripple Solutions' on Moving Finite Element Meshes*, IEEE Trans. on Magn., Vol. 31, No. 3, pp. 1472-1475, May 1995.

[4] T. Weiland, *A Discretization Method for the Solution of Maxwell's Equations for six-component Fields*, AEÜ Archiv für Elektrotechnik und Übertragungstechnik, Band 31, pp. 116-120, 1977.

[5] T. Weiland, *A Numerical Method for the Solution of the Eigenwave Problem of Longitudinally Homogeneous Waveguides*, AEÜ Archiv für Elektrotechnik und Übertragungstechnik, Band 31, pp. 308-314, 1977.

[6] T. Weiland, *Lossy Waveguides with an Arbitrary Boundary Contour and Distribution of Material*, AEÜ Archiv für Elektrotechnik und Übertragungstechnik, Band 33, pp. 170-174, 1979.

[7] PASIM Direktantriebe GmbH, http://www.direktantriebe.com/.

[8] http://maxwell.byu.edu/ spencerr/phys442/node4.html.

[9] J. Jeans, *The Mathematical Theory of Electricity and Magnetism*, Cambridge University Press, 1951.

[10] R.H. Atkin, *Theoretical Electromagnetism*, Printed in Northern Ireland at The University Press, 1962.

[11] W.H. Hayt,JR., *Engineering Electromagnetics*, McGraw-Hill Book Company, Inc., USA, 1958.

[12] R. Plonsey, R.E. Collin, *Principles and Applications of Electromagnetic Fields*, McGraw-Hill Book Company, Inc., USA, 1961.

[13] J.A. Stratton, *Electromagnetic Theory*, McGraw-Hill Book Company, Inc., USA, 1941.

[14] M. Mason and W. Weaver, *The Electromagnetic Field*, Dover Publications, Inc., New York, 1929.

[15] H. De Gersem, *Simulation of Field-circuit Coupled Motional Eddy Current Problems by Krylov Subspace Methods and Multilevel Techniques*, Dissertation, Katholieke Universiteit Leuven, 2001.

[16] A. Binder, *Electrical Machines and Drives I.*, Skriptum zur Vorlesung, TU Darmstadt, 2004.

[17] D. Ioan, *Modelarea Dispozitivelor Electromagnetice*, notite de curs, Facultatea de Electrotehnica, Universitatea Politehnica Bucuresti.

[18] J.R. Reitz, *Foundation of Electromagnetic Theory*, Addison-Wesley Publishing Company, Inc., USA, May 1962.

[19] T. Weiland, *Elektromagnetisches CAD - Rechnergestützte Methoden zur Berechnung von Feldern*, Skriptum zur Vorlesung Feldtheorie II, TU-Darmstadt, 1998.

[20] T. Weiland, *On the Unique Numerical Solution of Maxwellian Eigenvalue Problems in Three Dimensions*, Particle Accelerators, Vol. 17, pp. 227-242. 1985.

[21] T. Weiland, *Time Domain Electromagnetic Field Computation with Finite Difference Methods*, Int. J. Num. Mod.: Electronic Networks, Devices and Fields, Vol. 9, pp. 295-319, 1996.

[22] T. Weiland, *Zur numerischen Lösung des Eigenwellenproblems längshomogener Wellenleiter beliebiger Randkorrektur und transversal inhomogener Füllung*, Dissertation, Technische Hochschule Darmstadt, 1977.

[23] M. Clemens, S. Feigh, T. Weiland, *Geometric Multigrid Algorithms Using the Conformal Finite Integration Technique*, IEEE Trans. on Magn., Vol. 40, No. 2, Part 2, pp. 1065 - 1068, March 2004.

[24] http://www.colorado.edu/engineering/CAS/courses.d
/AFEM.d/AFEM.Ch05.d/AFEM.Ch05.Slides.d/AFEM.Ch05.Slides.pdf.

[25] R. Magureanu, N. Vasile, *Motoare Sincrone cu Magneti Permanenti si Reluctanta Variabila*, Editura Tehnica, Bucuresti, 1982.

[26] I. Boldea, *Reluctance Synchronous Machines and Drives*, Clarendon Press, Oxford, 1996.

[27] J.P.A. Baston, N. Sadowski, *Electromagnetic Modeling by Finite Element Methods*, Marcel Dekker, Inc. 2003.

[28] U.v. Rienen, *Numerical Methods in Computational Electrodynamics*, Springer-Verlag, 2001.

[29] T. Nakata, N. Takahashi, K. Fujiwara, A. Ahagon, *Periodic Boundary Condition for 3-D Magnetic Field Analysis and its Applications to Electrical Machines*, IEEE Trans. on Magn., Vol. 24, No. 6, pp. 2694-2696, 1988.

[30] P.J. Leonard, H.C. Lai, P.R.J. Hill-Cottingham, *Treatment of Symmetry in Three Dimensional Finite Element Models of Machines Coupled to External Circuits* , IEEE Trans. on Energy Conversion, Vol. 14, No. 4, pp. 1276-1281, 1999.

[31] Computer Simulation Technology GmbH, http://www.cst.com/.

[32] N. Sadowski, Y. Lefevre, M. Lajoie-Mazenc, J. Cross, *Finite Element Torque Calculation in Electrical Machines while Considering the Movement*, IEEE Trans. on Magn., Vol. 28, No. 2, pp. 1410-1413, 1992.

[33] R. Perrin-Bit, *A Three Dimensional Finite Element Mesh Connection for Problems Involving Movement*, IEEE Trans. on Magn., Vol. 31, No. 3, pp. 1920-1923, May 1995.

[34] A. Demenko, *Movement Simulation in Finite Element Analysis of Electrical Machine Dynamics*, IEEE Trans. on Magn., Vol. 32, No. 3, pp. 1553-1556, May 1996.

[35] Y. Saad, *Iterative Methods for Sparse Linear Systems*, PWS Publishing Company, 1996; http://www-users.cs.umn.edu/ saad/books.html.

[36] H.A. van der Vorst, *Iterative Krylov Methods for Large Linear Systems*, Cambridge University Press, 2003.

[37] L. Lapidus, G.F. Pinder, *Numerical Solution of Partial Differential Equations in Science and Engineering*, John Wiley and Sons, 1982.

[38] J.M. Ortega and W.C. Rheinboldt, *Iterative Solution of Nonlinear Equations in Several Variables*, Academic Press, Inc. San Diego, California, 1970.

[39] H. De Gersem, T. Weiland, *A Computationally Efficient Air-Gap Element for 2D FE Machine Models*, IEEE Trans. on Magn., Vol. 41, No. 5, pp. 1844-1847, May 2005.

[40] T.W. Preston, A.B.J. Reece, and P.S. Sangha, *Induction Motor Analysis by Time-stepping Techniques*, IEEE Trans. on Magn., Vol. 24, No. 1, pp. 471-474, Jan. 1988.

[41] F. Rapetti, F. Bouillault, L. Santandrea, A. Buffa, Y. Maday, and A. Razek, *Calculation of Eddy Currents with Edge Elements on Non-matching Grids in Moving Structures*, IEEE Trans. on Magn., Vol. 36, No. 4, pp. 1351-1355, July 2000.

[42] Y. Maréchal, G. Meunier, J.L. Coulomb, and H. Magnin, *A General Purpose Tool for Restoring Inter-element Continuity*, IEEE Trans. on Magn., Vol. 28, No. 2, pp. 1728-1731, Mar. 1992.

[43] H. De Gersem, T. Weiland, *Harmonic Weighting Functions at the Sliding Interface of a Finite-element Machine Model Incorporating Angular Displacement*, IEEE Trans. on Magn., Vol. 40, No. 2, pp. 545-548, Mar. 2004.

[44] H. De Gersem, M. Wilke, M. Clemens and T. Weiland, *Efficient Modeling Techniques for Complicated Boundary Conditions Applied to Structured Grids*, COMPEL, Vol. 23, pp. 904–912, 2004.

[45] J. Yuan, *Numerical Simulation of Hysteresis Effects in Ferromagnetic Material with the Finite Integration Technique*, Cuvillier Verlag, Göttingen, 2005.

[46] D.M. Young, *Historical overview of iterative methods*, Practical Iterative Methods for Large Scale Computations, Minneapolis, USA, pp. 1-17, 23-25 Oct 1988.

[47] A. Greenbaum, *Iterative Methods for Solving Linear Systems*, Society for Industrial and Applied Mathematics, 1997.

[48] M.R. Hestenes, E. Stiefel, *Methods of Conjugate Gradients for Solving Linear Systems*, Journal of Research of the National Bureau Standards, Vol. 49, pp. 409-436, 1952.

[49] C. Wagner, *Introduction to Algebraic Multigrid*, Course Notes of an Algebraic Multigrid.

[50] B. Wohlmuth, *Discretization Methods and Iterative Solvers Based on Domain Decomposition*, Springer, 2001.

[51] R. Mertens, U. Pahner, K. Hameyer and R. Belmans, *Force Calculation Based on a Local Solution of Laplace's Equation*, IEEE Trans. on Magn., Vol. 33, No. 2, pp. 1216-1218, 1997.

[52] U. Pahner, *A General Design Tool for the Numerical Optimisation of Electromagnetic Energy Transducers*, Dissertation, Katholieke Universiteit Leuven, 1998.

[53] J.R. Brauer and J.J. Ruehl, *3D Coupled Electromagnetic and Structural Finite Element Analysis of Motional Eddy Current Problems*, IEEE Trans. on Magn., Vol. 30, No. 5, pp. 3288 - 3291, September 1996.

[54] A. Nicolet, *Implicit Runge-Kutta Method in Magnetodynamic Problems*, COMPEL, Vol. 16, pp. 49-55, 1997.

[55] A. Balahcen, *Overview of the Calculation Methods for Forces in Magnetised Iron Cores of Electrical Machines*, Helsinki University of Technology, Laboratory of Electromechanics, 1999.

[56] A. Balahcen, *Magnetic Forces Calculation for Noise Analysis of Electrical Machines*, Helsinki University of Technology, Laboratory of Electromechanics.

[57] Du-Suk. Heo, Kyu-Hwan Hwang, Yun-Hyun Cho, *The Analysis of the Vibration Characteristics of a Linear Pulse Motor According to Input Current Waves*, Proceedings of the 16th International Conference on Electrical Machines (ICEM'04), Cracow, Poland, 05.-08.09.04, pp. 703-704, 2004.

[58] M. Gabsi, X. Mininger, Y. Bonnassieux, T. Poux, B. Grioni, *Indirect Vibration Sensors for Switched Reluctance Motors*, Proceedings of the 16th International Conference on Electrical Machines (ICEM'04), Cracow, Poland, 05.-08.09.04, on CD, 2004.

[59] T.J.E. Miller, *Switched Reluctance Motors and Their Control*, Magna Physics Publishing and Clarendon Press, Oxford, 1993.

[60] M. Wilke, *Zur numerischen Berechnung quasistationärer elektromagnetischer Felder im Zeitbereich*, Dissertation, Technische Universität Darmstadt, 2004.

[61] S. Drobny, T. Weiland, *Numerical Calculation of Nonlinear Transient Field Problems with the Newton-Raphson Method*, IEEE Trans. on Magn., Vol. 36, pp. 809-812, 2000.

[62] S. Drobny, M. Clemens, T. Weiland, *Dual Nonlinear Magnetostatic Formulations Using the Finite Integration Technique*, Conference Records of the IEEE Conference on Electromagnetic Field Computation (CEFC 2000), Milwaukee, USA, p. 392, 2000.

[63] P. Deuflhard, *Newton Methods for Nonlinear Problems*, Springer - Verlag Berlin Heidelberg 2004.

[64] H. De Gersem, I. Munteanu and T. Weiland, *Comparison of Newton and Approximate Newton Methods for the Orthogonal Finite Integration Technique.* Presented at Scientific Computing in Electrical Engineering (SCEE06), Sinaia, Romania 2006.

[65] A.K. Daud, R. Hanitsch, *Design of Hybrid Linear Stepping Motor (HLSM) for Long Stroke Operation*, Proceedings of the 16th International Conference on Electrical Machines (ICEM'04), Cracow, Poland, 05.-08.09.04, on CD, 2004.

Publications and presentations (*My birth name is Mariana Ion and the papers are published under this name until my marriage in 2005, when I took the name Funieru.*)

[66] M. Ion, H. De Gersem, and T. Weiland, *Electrical machine simulation by the Finite Integration Technique using cylindrical coordinates*, Graduiertenkolleg "Modellierung, Simulation und Optimierung von Ingenieuranwendungen", Annual Meeting, Lambrecht, Germany, November 24-25, 2003.

[67] M. Ion, H. De Gersem, and T. Weiland, *Sliding-Surface Interface Conditions for 3D Models discretised by FIT*, Graduiertenkolleg "Modellierung, Simulation und Optimierung von Ingenieuranwendungen", Annual Meeting, Seeheim, Germany, December 9-10, 2004.

[68] M. Ion, H. De Gersem, and T. Weiland, *Sliding-surface interface conditions for 3D machine models discretised by FIT*, Workshop Computational Engineering Forschung und Lehre, Darmstadt, Germany, February 23-24, 2005.

[69] M. Ion, H. De Gersem and T. Weiland, *Sliding-Surface Interface Conditions and Force Calculation for a Linear Actuator Discretised by the Finite Integration Technique*, Studies in Applied Electromagnetics and Mechanics (Electromagnetic Field in Mechatronics, Electrical and Electronic Engineering, Proceedings of ISEF'05), Volume 27, pp. 185–192, 2006.

[70] H. De Gersem, M. Ion and T. Weiland, *Trigonometric Interpolation at Sliding Surfaces and in Moving Bands of Electrical Machine Models*, COMPEL, Volume 25, No. 1, pp. 31–42, 2006.

[71] M. Ion, H. De Gersem, M. Wilke and T. Weiland, *Sliding-Surface Interface Conditions for 3D Machine Models Discretised by the Finite Integration Technique*, COMPEL, Vol. 25, No. 2, pp. 427-439, 2006.

[72] M. Funieru, H. De Gersem and T. Weiland, *Transient Simulation of a Linear Actuator discretised by the Finite Integration Technique*, The 6th Conference on Scientific Computing in Electrical Engineering, SCEE 2006, Sinaia, Romania, 17 - 22 September 2006.

Acknowledgements

I would like to express my gratitude to all the people, who directly or indirectly helped me in various ways throughout the preparation and release of this Ph.D. work, as well as the Graduiertenkollegs "Modellierung, Simulation und Optimierung von Ingineureandwendungs" and Forschungszentrums Computational Engineering for providing me the grant for all 4 years of study.

- First of all, I would like to express my sincere gratitude to Prof. Dr.-Ing. Thomas Weiland, for the scientific supervision and the opportunities he created for me by enroling me at the *Institut für Theorie Electromagnetischer Felder, Technische Universität Darmstadt*, and making possible for me to successfully complete my Ph.D. work.
- I would like to thank Prof. Dr.-Ing. Daniel Ioan for his support as co-referee. It is also my great pleasure to thank him again for being a very good guide as chef of the Numerical Laboratory, where I made my specialization.
- Special thanks to Dr.-Ing. Herbert De Gersem for being my supervisor, for his scientific guidance and correcting this dissertation. I have learned a lot from him, not only the careful and diligent research attitude.
- During the research activities at TEMF, my present and former colleagues provided the pleasant and friendly atmosphere. Other special thanks to Prof. Dr.-Ing. Irina Munteanu, who gave me a lot of helpfully advices, Frau Dagmar Stenger who helped me to adapt to German life, as well as to Heike Seiler for her patience to translate me all the German notes.
- I want to express my deeply thanks to my husband Dipl.-Ing Bogdan Funieru for his day-by-day support.

Curriculum Vitae - Mariana Funieru

Birth name: Ion

25.02.1978	• Born in Bucharest / Romania
1984-1992	• The No. 46 General School in Bucharest
1992-1996	• Industrial Electronic Highschool in Bucharest
1996-1997	• First year of Nursing School
1997-2002	• Dipl.-Ing. degree study at Department of Electrical Engineering, University 'Politehnica' Bucharest; (March - May 2002) Diploma Thesis 'Modelling of the System inverter-cable-motor to predict inductively coupled bearing currents for power levels up to 500 kW' at Institut für Elektrische Energiewandlung of Technischen Universität Darmstadt
2003-2006	• Research assistant at Institut für Theorie Elektromagnetischer Felder of Technischen Universität Darmstadt
2005	• Married with Bogdan-Ion Funieru.